

# Nonlithographic Formation of Ta<sub>2</sub>O<sub>5</sub> Nanodimple Arrays Using Electrochemical Anodization and Their Use in Plasmonic Photocatalysis for Enhancement of Local Field and Catalytic Activity

Ryan Kisslinger,\* Saralyn Riddell, Ajay P. Manuel, Kazi M. Alam, Aarat P. Kalra, Kai Cui, and Karthik Shankar\*

Cite This: *ACS Appl. Mater. Interfaces* 2021, 13, 4340–4351

Read Online

ACCESS |

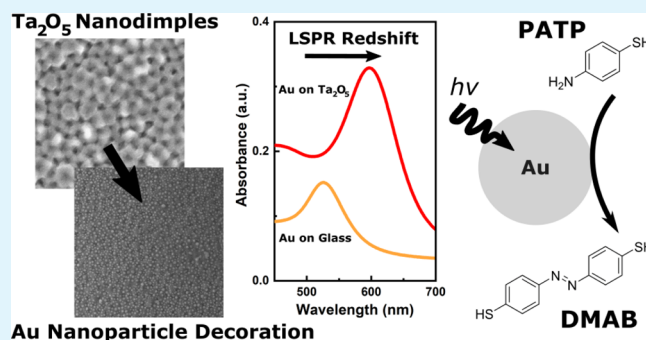
Metrics & More

Article Recommendations

Supporting Information

**ABSTRACT:** We demonstrate the formation of Ta<sub>2</sub>O<sub>5</sub> nanodimple arrays on technologically relevant non-native substrates through a simple anodization and annealing process. The anodizing voltage determines the pore diameter (25–60 nm), pore depth (2–9 nm), and rate of anodization (1–2 nm/s of Ta consumed). The formation of Ta dimples after delamination of Ta<sub>2</sub>O<sub>5</sub> nanotubes occurs within a range of voltages from 7 to 40 V. The conversion of dimples from Ta into Ta<sub>2</sub>O<sub>5</sub> changes the morphology of the nanodimples but does not impact dimple ordering. Electron energy loss spectroscopy indicated an electronic band gap of 4.5 eV and a bulk plasmon band with a maximum of 21.5 eV. Gold nanoparticles (Au NPs) were coated on Ta<sub>2</sub>O<sub>5</sub> nanodimple arrays by annealing sputtered Au thin films on Ta nanodimple arrays to simultaneously form Au NPs and convert Ta to Ta<sub>2</sub>O<sub>5</sub>. Au NPs produced this way showed a localized surface plasmon resonance maximum at 2.08 eV, red-shifted by ~0.3 eV from the value in air or on SiO<sub>2</sub> substrates. Lumerical simulations suggest a partial embedding of the Au NPs to explain this magnitude of the red shift. The resulting plasmonic heterojunctions exhibited a significantly higher ensemble-averaged local field enhancement than Au NPs on quartz substrates and demonstrated much higher catalytic activity for the plasmon-driven photo-oxidation of *p*-aminothiophenol to *p,p'*-dimercaptoazobenzene.

**KEYWORDS:** self-organization, nanopore arrays, anodic synthesis, plasmon-mediated chemical reactions, SERS, FDTD simulations



## 1. INTRODUCTION

Anodization of metals such as Al, Ti, Ta, Ni, Fe, and so forth has proven to be an effective method to produce ordered nanostructured surfaces.<sup>1–5</sup> Furthermore, this solution-processable method is known to be suitable for industrial-scale production; this is demonstrated in the production of alumina coatings. Anodically formed nanostructured metal and metal oxide surfaces have numerous uses—from superior wear and corrosion resistance to serving as a base layer for the production of fouling resistant surfaces and to optical and electronic applications.<sup>6–9</sup> Tantalum nanodimples can be obtained by electrochemical means, including electropolishing and delamination of grown nanotubes in an anodization process.<sup>10–14</sup> Typically, these dimples appear as regular concavities across the surface and have diameters in tens of nanometers and depths of ca. 10 nm. These dimples have been observed in several studies, but to date, they have barely been investigated. To the best of our knowledge, the only studies that are dedicated to this topic were conducted by El-Sayed et al. who investigated the dimples' use as nanostructured electrodes.<sup>13</sup>

The conversion of the Ta nanodimples to its analogous oxide or nitride opens up a huge array of applications for the nanodimples, such as serving as a base for UV-transparent superhydrophobic coatings, as the active layer in photodiodes for charged particle radiation detection,<sup>15</sup> as a photocatalyst<sup>16</sup> and electrocatalyst<sup>17</sup> to leverage the simultaneously high oxidizing and reducing power of photogenerated holes and electrons, as a catalyst for the rate capability enhancement of lithium sulfur batteries,<sup>18</sup> as a platform for plasmonic hot carrier devices,<sup>19</sup> and so forth. In fact, there has recently been a revival of research interest in the electronic and optoelectronic applications of ultrawide band gap materials with semiconducting properties such as Ga<sub>2</sub>O<sub>3</sub>, Ta<sub>2</sub>O<sub>5</sub>, GeO<sub>2</sub>, and BN.<sup>20–26</sup>

Received: October 16, 2020

Accepted: January 5, 2021

Published: January 17, 2021



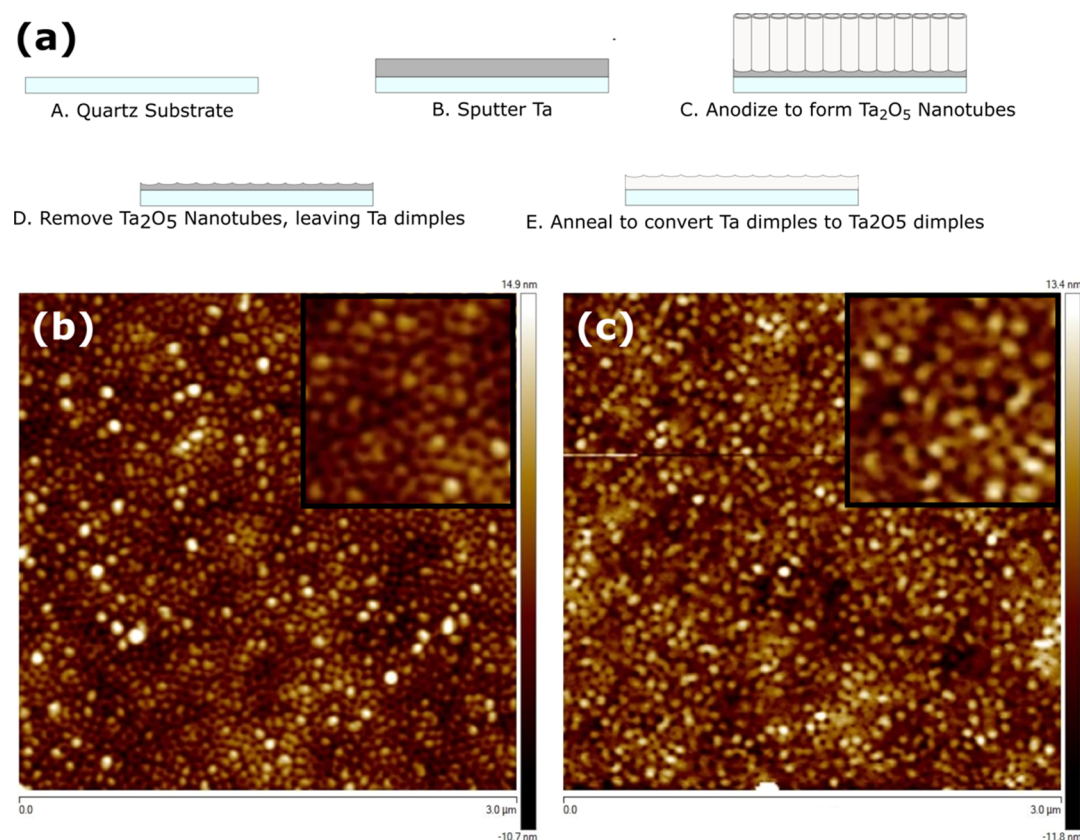


**Figure 1.** (a) Schematic illustration of the growth of Ta<sub>2</sub>O<sub>5</sub> nanodimples on a quartz substrate. (b,c) Characteristic AFM images of (b) Ta nanodimples and (c) Ta<sub>2</sub>O<sub>5</sub> nanodimples. The insets in (b,c) display a magnified version of the AFM images; the horizontal field of view for both insets is 690 nm. Both sets of AFM images were collected from Ta films anodized at 20 V.

In this work, the production of Ta<sub>2</sub>O<sub>5</sub> nanodimple arrays on technologically relevant non-native substrates is described. The morphological changes during annealing-induced transformation of Ta to Ta<sub>2</sub>O<sub>5</sub> are minor, and the ordering of the dimples is maintained. We also demonstrate that oxide conversion of the dimples is possible via anodization to avoid the elevated temperatures involved in the annealing process. We conduct a comparison of structural dimensions across differing anodization voltages and quantify the morphological changes that are expected after annealing using electron and helium ion microscopy (HIM) and atomic force microscopy (AFM). X-ray diffraction (XRD) and energy-dispersive X-ray spectroscopy (EDX) provide further support of the effects of annealing. We then turn to potential uses of the Ta<sub>2</sub>O<sub>5</sub> nanodimples as platforms for plasmonic photocatalysis by forming heterojunctions with Au nanoparticles (NPs). We utilize ultraviolet–visible (UV–vis) spectroscopy to demonstrate the absorption characteristics of these samples before and after Au NP formation to show the clear effects that localized surface plasmon resonance (LSPR) causes in the absorption profile and, in tandem with electron energy loss spectroscopy (EELS), quantify the optical band gap of the Ta<sub>2</sub>O<sub>5</sub>. We demonstrate a red shift of the LSPR of Au NPs on Ta<sub>2</sub>O<sub>5</sub> nanodimples only fully achievable through a simultaneous formation of NPs and oxide growth in a single annealing procedure. Lumerical simulations are utilized to demonstrate the optical effects of dimple morphology and strongly suggest that gold NPs are at least partially embedded into the oxide. Finally, utilizing surface-enhanced Raman spectroscopy (SERS), we demonstrate that Ta<sub>2</sub>O<sub>5</sub> nanodimples are able to increase the

photocatalytic conversion rate of *para*-aminothiophenol (PATP) to *p,p'*-dimercaptoazobenzene (DMAB) when used in tandem with Au NPs.

## 2. EXPERIMENTAL SECTION

**2.1. Fabrication of Nanodimple Arrays.** A schematic of the process flow used to form the nanodimples formed in this study is shown in Figure 1a. The substrates were fused quartz slides purchased from Advalue Technologies. Ta thin films were vacuum-deposited on quartz by DC magnetron sputtering using a Ta target of 99.95% purity (Kurt J. Lesker). Before sputtering, the substrates were immersed for 15 min in a piranha solution composed of a 3:1 mixture of sulfuric acid and hydrogen peroxide and then rinsed with deionized (DI) H<sub>2</sub>O and dried under flowing nitrogen. All sputtering was conducted in an argon-filled chamber at 2.5 mTorr using a power of 200 W with a target-to-substrate distance of 15 cm. The low chamber pressure exploited the atomic peening mechanism to enhance the smoothness and density of Ta films.<sup>27</sup> The substrate was heated to 500 °C during deposition, and the deposition rate was 1.28 Å s<sup>-1</sup>, as measured by a quartz crystal monitor. The electrolyte used for anodization consisted of 0.24 M NH<sub>4</sub>F in a solution containing 5 vol % DI H<sub>2</sub>O, 5 vol % diethylene glycol (DEG), and 90 vol % sulfuric acid (H<sub>2</sub>SO<sub>4</sub>, 95–98%). This electrolyte was prepared by first dissolving NH<sub>4</sub>F in H<sub>2</sub>O and then adding DEG. Concentrated sulfuric acid was subsequently slowly added in and stirred, and the as-formed solution was allowed to cool to room temperature (the addition of H<sub>2</sub>SO<sub>4</sub> being exothermic). The cathode was a 3.05 mm-diameter carbon rod submerged 2 cm into the electrolyte. The anode was spaced 1 cm below this cylindrical carbon rod, and the anodized area was 16 mm<sup>2</sup>. No reference electrode was used, and anodization was conducted potentiostatically without stirring. After anodization, the sample was removed from the electrolyte and submerged in DI water to remove the formed nanotubes through mechanical stress and

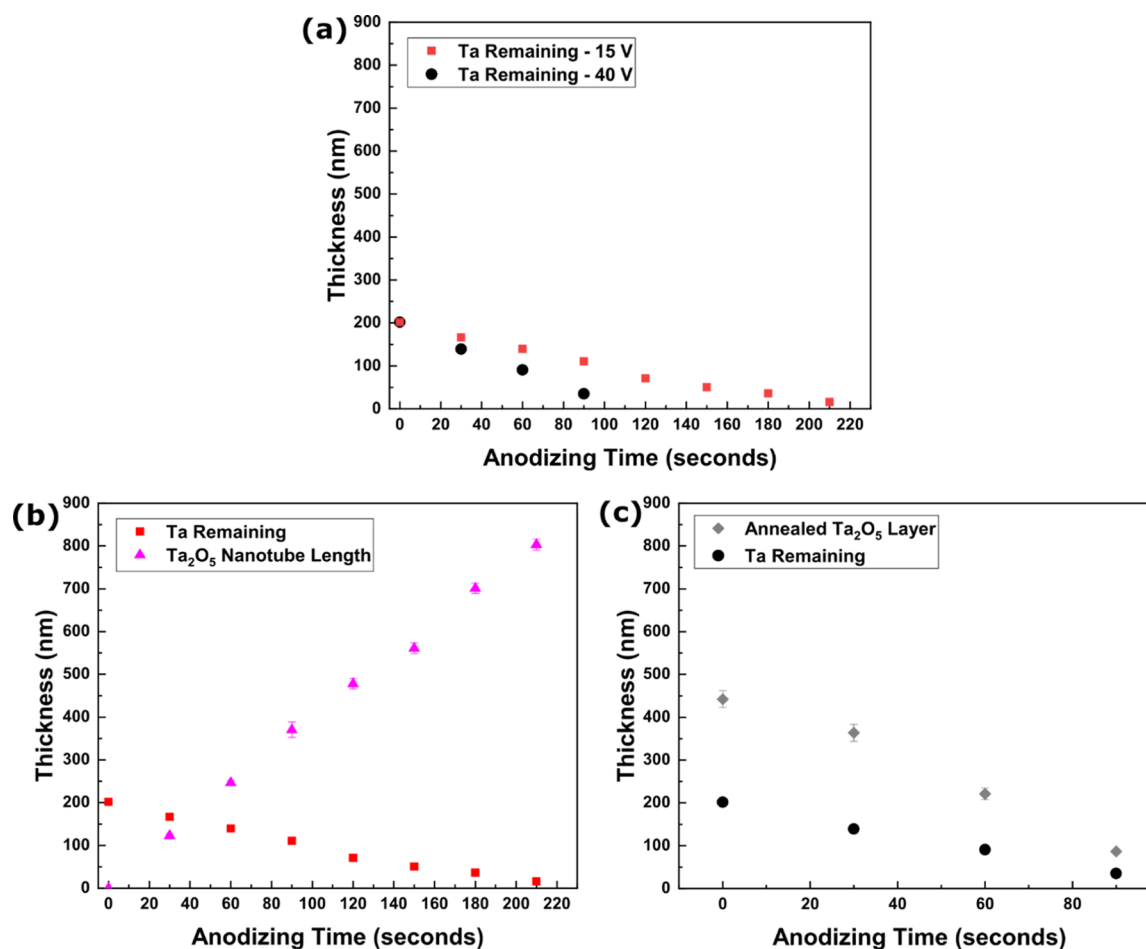


**Figure 2.** Film thicknesses as a function of anodizing time. (a) Consumption of 200 nm Ta films under anodization at both 15 and 40 V synthesis voltages. (b) Growth of nanotube length and the corresponding tantalum consumed at 15 V. (c) Conversion of a nanodimpled Ta film into a Ta<sub>2</sub>O<sub>5</sub> film after annealing at 40 V. Note that (b), in part, displays identical data as the “Ta remaining—15 V” data points from (a) and (c), in part, displays identical data as the “Ta remaining—40 V” data points from (a).

wetting-induced spontaneous delamination; this also served to rinse away the residual electrolyte. After drying under a nitrogen jet, samples were placed in a tube furnace for annealing. Annealing to convert bare Ta nanodimples to Ta<sub>2</sub>O<sub>5</sub> nanodimples was conducted at 650 °C for 3 h, with a 3 h ramp up time from room temperature.

**2.2. Characterization.** The morphology of the samples was imaged using either a Zeiss Sigma field emission scanning electron microscope or a Zeiss Orion helium ion microscope; the advantage of HIM in certain situations was to achieve greater topological information when the low-voltage field emission scanning electron microscopy (FESEM) imaging was restrictive. When using HIM, an electron flood gun could be used to neutralize sample charging. The pore diameters were measured from acquired micrographs using ImageJ software. The diameter of each pore was measured as the farthest distance a horizontal line could pass from the left to right pore edge. For pore selection, a single pore was initially selected arbitrarily near the center of an FESEM micrograph, with subsequent pores being chosen in an outward spiral from the starting pore. In all cases, 100 pores were measured. Two-dimensional fast Fourier transforms (2D-FFT) of the FESEM images were obtained using WSxM software.<sup>28</sup> EDX analysis was conducted using the mentioned FESEM alongside an Oxford X-max system, and the spectra were analyzed using Oxford AZtec software. AFM images were collected using a Bruker Dimension Edge atomic force microscope. The instrument was operated in the tapping mode and used a tip of <10 nm atomic radius. Dimple depth was measured by considering the vertical depth of a pore from the sidewall to the lowest point in the middle of a pore; pore selection was carried out in an identical fashion to pore diameter,

and 100 pores were measured. X-ray diffractograms were collected using a Rigaku Ultima IV equipped with a Cu K $\alpha$  source. The EELS spectra were acquired using a Hitachi H9500 transmission electron microscope with an accelerating voltage of 300 kV and were recorded on a Gatan GIF Tridium spectrometer. The zero-loss peak was subtracted for the Ta<sub>2</sub>O<sub>5</sub> spectrum; the electron counts for the Ta spectrum were normalized to the Ta<sub>2</sub>O<sub>5</sub> spectrum by dividing the actual measured counts by 15. UV–vis spectra were obtained using a PerkinElmer Lambda 1050 spectrophotometer.

**2.3. FDTD Electromagnetic Simulations.** Finite difference time domain (FDTD) electromagnetic simulations were used to model the optical properties of the Ta<sub>2</sub>O<sub>5</sub> nanodimples using Lumerical FDTD simulation software. The optical absorption and scattering of nanodimples with a pore diameter of 30 nm and a pore depth of 5 nm, corresponding to an anodization voltage of 30 V, were simulated. Three sets of simulations were performed, each exploring the effect of the high-index Ta<sub>2</sub>O<sub>5</sub> dimpled dielectric substrate on gold NPs: (i) Au NPs partially embedded in a planar film of Ta<sub>2</sub>O<sub>5</sub>; (ii) Au NPs partially embedded in a Ta<sub>2</sub>O<sub>5</sub> nanodimple; and (iii) an array of Au NPs partially embedded in an array of Ta<sub>2</sub>O<sub>5</sub> nanodimples. The Au NPs were of radius 10 nm, and the simulations were performed in a vacuum environment. Index monitors were utilized to provide refractive index mapping of the simulated structures and helped confirm that the dimples and NPs were appropriately configured and identified by the software throughout the course of the simulation. Near-field and far-field profiles and frequency monitors captured reflection, transmission, scattering, and absorption spectra of the dimple–NP systems. Refractive index data corresponding to Ta<sub>2</sub>O<sub>5</sub>

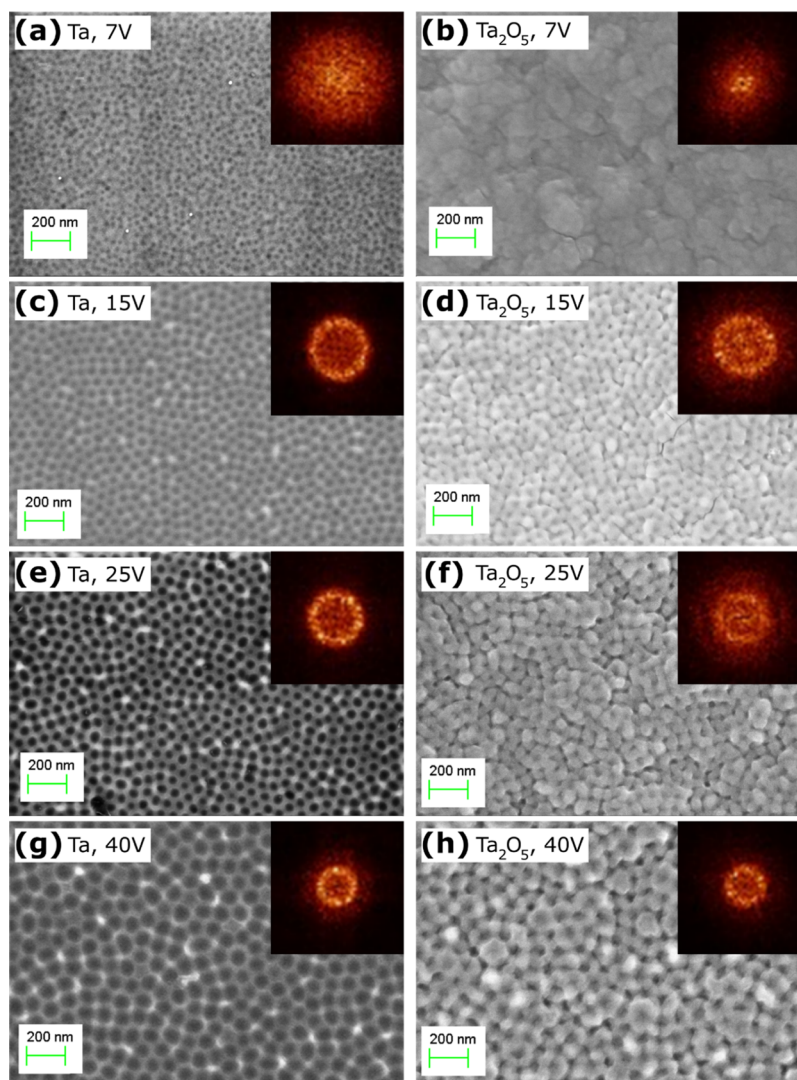


**Figure 3.** SEM images of nanodimples. Insets show 2D-FFT images (a,c,e,g) of Ta dimples (left side column), while (b,d,f), and (h) are 2D-FFT images of  $\text{Ta}_2\text{O}_5$  dimples (right side column). Anodization voltages correspond as follows: (a,b) 7 V, (c,d) 15 V, (e,f) 25 V, and (g,h) 40 V.

were obtained from Rodríguez-de Marcos et al.<sup>29</sup> The dimples were illuminated at normal incidence by a plane-wave light source with a 250–800 nm bandwidth. The symmetry of the  $\text{Ta}_2\text{O}_5$  nanodimples was exploited by setting appropriate symmetric and anti-symmetric boundaries, allowing for shorter simulation times and accurate data aggregation.

**2.4. Au NP Preparation and Photocatalytic Activity Tests.** Au NPs (NPs) were prepared by first using DC magnetron sputtering to deposit Au thin films on the substrate of interest. The deposition parameters were as follows: the base pressure was  $10^{-6}$  Torr, argon was used as the sputtering gas, the deposition pressure was 7 mTorr, and the deposition power was 75 W. Sputter deposition was performed for 20 s at a rate of  $\sim 7.6$  nm  $\text{min}^{-1}$  using a 75 mm-diameter 99.9% purity Au sputtering target. No substrate heating was used during gold deposition. Except where specifically noted, the substrate used was a Ta nanodimple array prepared by the anodization process described above at a voltage of 20 V. Thermal annealing was then conducted in a tube furnace in air at 650 °C for 30 min, with a 1 h ramp up time from room temperature; in the case of Au film-coated Ta nanodimples, this process was used to simultaneously transform the Ta nanodimples to  $\text{Ta}_2\text{O}_5$  nanodimples and form Au NPs by spontaneous thermal dewetting. The diameters of the Au NPs were obtained by the same procedure as described for the pore diameter. The samples were prepared for photocatalytic studies by drop-coating 1 mL of a solution of 50  $\mu\text{M}$  of PATP in

methanol on the sample substrates. The photocatalytic reaction was powered by the 633 nm red laser of a Nicolet Omega XR Raman microscope and a laser illumination power of 0.1–2 mW, which simultaneously collected Raman spectra and allowed for immediate feedback regarding the reaction products. Spectra acquired at using different illumination powers were tested on different spots across a sample using a 50  $\mu\text{m}$  confocal pinhole aperture slit. The reaction time (which was also the Raman spectra acquisition time) was 60 s.

### 3. RESULTS AND DISCUSSION

**3.1. Formation of  $\text{Ta}_2\text{O}_5$  Nanodimples.** Anodization of Ta films at voltages between 7 and 40 V resulted in the formation of  $\text{Ta}_2\text{O}_5$  nanotube arrays (Figure S1 in the Supporting Information). Extending the voltage beyond this range (experiments were conducted at 45, 50, 60, and 80 V) results in a disordered porous oxide, in agreement with the findings of Singh et al.<sup>30</sup> Figure 1b shows an AFM image of Ta nanodimples formed by delamination of  $\text{Ta}_2\text{O}_5$  nanotubes anodized at 20 V, while Figure 1c shows the corresponding  $\text{Ta}_2\text{O}_5$  nanodimples after annealing in air. The current densities were recorded as a function of time during the anodization process and are shown in Figure S2 in the Supporting Information. The curves are typical of a nanotube

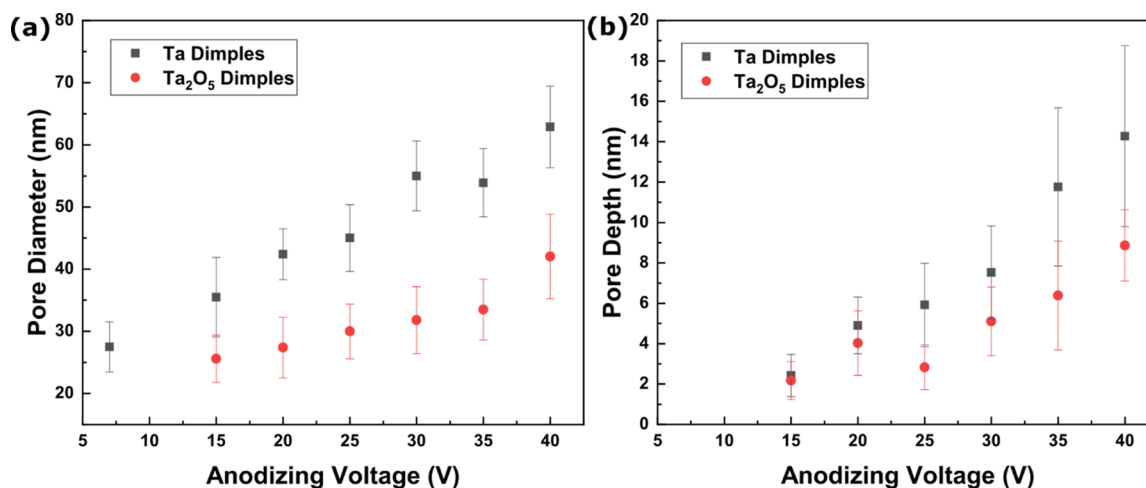


**Figure 4.** (a) Pore diameter and (b) pore depth of nanodimples as a function of anodization voltage, before and after annealing.

anodization process with the following characteristic features: (i) an initial rapid decrease in current as oxide forms on the surface through field-assisted oxidation, which acts as a barrier to the flow of electrons, while allowing a small ionic current; (ii) an increase in current as the oxide thins locally owing to pore formation mediated by field-assisted dissolution of the oxide; (iii) a steady decrease in current due to mass transport limitations as the nanotubes grow longer, meaning that ions must diffuse farther from the bulk to take part in the anodization reaction. Abnormally, two small increases in current are observed between 20 and 35 s using higher voltages; they can possibly be attributed to a shift from a disordered pore formation to a self-organized one that occurs during initial anodizing steps<sup>31</sup> or an increase in temperature leading to a faster reaction rate that occurs during the exothermic anodization process.

As anodization proceeds, Ta is consumed and the thickness of the vacuum-deposited Ta film decreases linearly, with higher voltages causing faster anodization. The cross-sectional thickness of the layers produced under differing conditions and after various anodization times was measured by FESEM, with the measured values reported in Figure 2. As shown in Figure 2a, Ta is consumed at rates of approximately 1.0 and 2.0 nm s<sup>-1</sup> for 15 and 40 V anodization, respectively. As the Ta is consumed, the length of the Ta<sub>2</sub>O<sub>5</sub> nanotubes (which may also be referred to as the thickness of the nanotube layer) increases correspondingly, at a rate of 3.8 nm s<sup>-1</sup> for 15 V, as is shown in Figure 2b. The length of the grown nanotubes far outstrips the amount of Ta consumed. This is partly explained by the volumetric expansion that occurs when a metal is converted to its metal/oxide analogue but not entirely. Conventionally, the Pilling–Bedworth ratio (PBR) relates the volume expansion of an oxide to its analogous metal.<sup>32</sup> Considering a 2D layer of the material, one can assume that all volumetric expansion occurs in the direction perpendicular to the substrate plane, meaning that the increase in layer thickness between Ta and Ta<sub>2</sub>O<sub>5</sub> can be directly related to the PBR. When oxide formation occurs at a metal/oxide interface, a volume change occurs due to the formation of the oxide.<sup>33</sup> This volume change depends on the metal and is calculated as

$$\Delta\text{PBR}_{\text{metal}} = \frac{V_{\text{m,oxide}}}{V_{\text{m,metal}}} = \frac{M_{\text{oxide}} \cdot \rho_{\text{metal}}}{n_{\text{atoms}} \cdot M_{\text{metal}} \cdot \rho_{\text{oxide}}} \quad (1)$$

where  $V_{\text{m,oxide}}$  and  $V_{\text{m,metal}}$  are the molar volume of the oxide and metal, respectively,  $M_{\text{oxide}}$  and  $M_{\text{metal}}$  are the atomic mass of the oxide and metal, respectively, and  $n_{\text{atoms}}$  is the number of atoms of metal per molecule of the oxide. The calculated ratio for Ta<sub>2</sub>O<sub>5</sub> is 2.47. We observe an average expansion ratio in layer thickness of 3.95 for Ta<sub>2</sub>O<sub>5</sub> nanotubes, far outpacing that expected for oxide expansion; this is explained by the porosity of the nanotube layer and the plastic flow model of the growth of cylindrical nanopores and nanotubes by anodization.<sup>34</sup> We note that our nanotubes appear to be either more dense or less porous than that obtained by Horwood et al. who noted an expansion ratio of 4.4.<sup>35</sup>

After removal of formed nanotubes, well-defined pores were found across the substrate. These pores are composed of Ta (as verified by XRD, EDX, and EELS later). However it should be noted that based on etch-depth X-ray electron spectroscopy investigations by El-Sayed et al., a thin layer of ~4 nm-thick amorphous Ta<sub>2</sub>O<sub>5</sub>—which is within the range that would be expected for the native oxide—is likely present on the surface.<sup>36</sup> After annealing, the Ta is converted into Ta<sub>2</sub>O<sub>5</sub>, as shown by XRD, EDX, and EELS later. We imaged the morphology of samples across a range of synthesis voltages both before and after annealing. The dimples enlarge as synthesis voltage increases. During annealing, the Ta is observed to expand during oxide formation. Consequently, the very small dimples obtained using an anodization voltage of 7 V disappear completely upon annealing. The ordering of the nanodimples is observed to be largely maintained across annealing, as evidenced by 2D-FFT results shown in the insets of Figure 3, a bright ring showing the presence of a short range order and disturbed long-term periodicity.<sup>37</sup> The samples made at 7 V show only a diffuse ring, indicating disorder across the sample surface. We also note that upon annealing, the entire layer thickness increases substantially owing to oxide expansion, as is shown in Figure 2c. Here, we note an expansion ratio of 2.43, which is well in line with the calculated PBR of 2.47.

The requirement of elevated annealing temperatures could present problems in some fabrication circumstances, for example, if silicon is the underlying substrate, at elevated annealing temperatures, silicon may be incorporated into the oxide film.<sup>38</sup> We conducted some brief exploration into using a second anodic oxidation instead of annealing to convert Ta nanodimples into Ta<sub>2</sub>O<sub>5</sub>, which we concluded was feasible.

These results are shared in Section S1 and Figure S3 in the Supporting Information.

Through analysis of FESEM and AFM images in Figures 1 and 3, we demonstrate control of the pore diameter and depth of the dimples by controlling the anodizing voltage, and both diameter and depth are shown to be an approximately linear function of the anodizing voltage (Figure 4). After annealing to form Ta<sub>2</sub>O<sub>5</sub>, the pore diameter and depth decrease as a result of oxide expansion. It should be noted, however, that it is possible that the AFM tip geometry and the relatively small lateral dimensions of the pores could have resulted in a measured pore depth that is less than the actual pore depth. Fresh tips were frequently used when acquiring measurements, and tips were of radius <10 nm, but nevertheless, we cannot entirely preclude a deeper pore depth than is measured.

**3.2. Characterization of Ta<sub>2</sub>O<sub>5</sub> Nanodimples.** XRD spectra of Ta and Ta<sub>2</sub>O<sub>5</sub> nanodimples are shown in Figure S4a,b in the Supporting Information. The peaks in the XRD spectrum were identified using powder diffraction files 00-046-1045, 00-004-0788, 04-011-3914, and 01-089-284 for quartz,  $\alpha$ -Ta,  $\beta$ -Ta, and  $\beta$ -Ta<sub>2</sub>O<sub>5</sub> respectively.<sup>39</sup> XRD confirms the presence of crystalline Ta prior to annealing; this spectrum is representative of Ta films obtained after sputtering but before any further processing. After annealing, we note the formation of crystalline Ta<sub>2</sub>O<sub>5</sub> but see no evidence of Ta. We also note that the broad peak attributed to the quartz substrate in Figure S4a appears to still be visible in Figure S4b, although a much stronger peak attributed to (001) Ta<sub>2</sub>O<sub>5</sub> mostly overlaps it. EDX spectra also confirm the presence of Ta before annealing and Ta<sub>2</sub>O<sub>5</sub> after annealing, as shown in Figure S5.

The EELS spectrum of Ta<sub>2</sub>O<sub>5</sub> shown in Figure 5 shows a very broad peak with its maximum at 21.4 eV, which

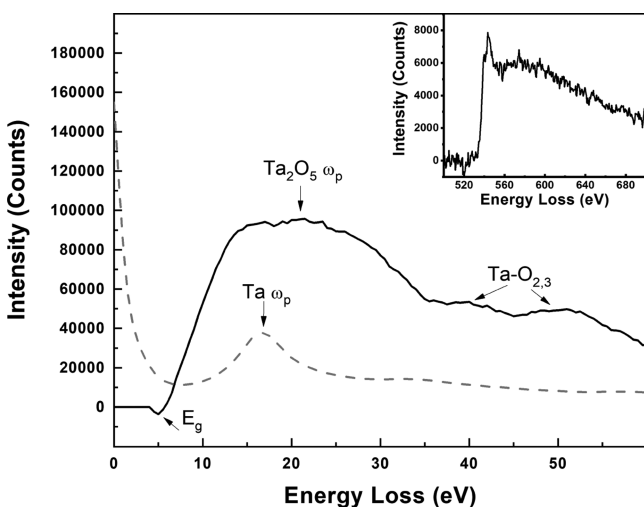


**Figure 5.** EELS spectrum of Ta<sub>2</sub>O<sub>5</sub> (black solid curve) and Ta (gray dashed curve), with the inset showing the O–K edge range of Ta<sub>2</sub>O<sub>5</sub>.

corresponds to the bulk plasmon oscillation frequency ( $\omega_p$ ) given by<sup>40</sup>

$$\omega_p^2 = \frac{ne^2}{m^* \epsilon_0}$$

where  $n$  is the number density of valence electrons in Ta<sub>2</sub>O<sub>5</sub>,  $e$  is the elementary charge,  $m^*$  is the carrier effective mass, and  $\epsilon_0$  is the permittivity of free space. In the range of energies corresponding to the bulk plasma resonance, the carrier

effective mass is expected to be close to the free electron mass due to the absence of electronic transitions.<sup>41</sup> Based on the specific volume of 88.27 Å<sup>3</sup> for the orthorhombic lattice<sup>42</sup> of  $\beta$ -Ta<sub>2</sub>O<sub>5</sub> and the O 2p<sup>4</sup> and Ta 5d<sup>3</sup>6s<sup>2</sup> valence shell configurations, the predicted bulk valence band plasmon frequency in  $\beta$ -Ta<sub>2</sub>O<sub>5</sub> is 21.5 eV, which closely matches the value obtained from the experimental EELS spectrum (Figure 5). The very broad bulk plasmon band is indicative of strong carrier scattering mechanisms (high plasmon damping) in Ta<sub>2</sub>O<sub>5</sub>, also observed in other reports.<sup>43</sup> The overall shape of the EELS spectrum closely resembles that of Ta<sub>2</sub>O<sub>5</sub> and differs noticeably from that of Ta, Ta coated with a native oxide and nonstoichiometric tantalum oxide; we note here a plasmon frequency of 16.9 eV for the unannealed Ta dimples, within the range expected for Ta.<sup>44–46</sup> Bands corresponding to the Ta–O<sub>2,3</sub> edge are also identified in the spectrum, which again confirms the presence of Ta in the sample. The band gap of the Ta<sub>2</sub>O<sub>5</sub>,  $E_g$ , can be estimated from the low energy threshold to be 4.5 eV, which falls within the range reported for Ta<sub>2</sub>O<sub>5</sub>.<sup>40</sup> The O–K edge is shown in the inset of Figure 5, with a typical edge onset of 532 eV, and peaks suggest similarity in pentoxide bonding characteristics for a Ta<sub>2</sub>O<sub>5</sub> material.<sup>47</sup>

**3.3. Au–Ta<sub>2</sub>O<sub>5</sub> Heterojunction Formation.** Figure 6a is an electron micrograph of Au NPs on Ta<sub>2</sub>O<sub>5</sub> nanodimple arrays; the presence of Au is confirmed by EDX spectra presented in Figure S5. The diameter of the Au NPs was measured to be 14.6 ± 2.8 nm. The UV–vis spectra (Figure 6b) show the optical extinction of the Ta<sub>2</sub>O<sub>5</sub> nanodimples with and without Au NPs. The Ta<sub>2</sub>O<sub>5</sub> nanodimple array exhibits a sharp band edge at ~300 nm in Figure 6b. In addition, some weak interference fringes are visible with crests at 309 and 474 nm and troughs at 382 and 692 nm. The fringes result from constructive and destructive interference of light reflected from the air–Ta<sub>2</sub>O<sub>5</sub> and Ta<sub>2</sub>O<sub>5</sub>–quartz interfaces.<sup>27</sup> The inset of Figure 6b shows the Tauc plot for the direct transition of Ta<sub>2</sub>O<sub>5</sub>, and we note a band gap of 4.5 eV (confirming the value obtained earlier from EELS). For Au NPs on Ta<sub>2</sub>O<sub>5</sub> nanodimple arrays, a distinct LSPR resonance appears at 600 nm (red curve in Figure 6b). This is a relatively long wavelength for plasmonic absorption for gold NPs in air or water, with plasmonic peaks usually centered around 510–530 nm for this size.<sup>48</sup> While the red shift of LSPR is typical for a higher dielectric constant environment around the Au NPs, the magnitude of the red shift is suggestive of Au NPs not merely located at the Ta<sub>2</sub>O<sub>5</sub>–air interface but being more substantially enveloped/surrounded by Ta<sub>2</sub>O<sub>5</sub>. Our results are remarkably similar to those obtained by Luo et al.,<sup>49</sup> who embedded Au NPs in Ta<sub>2</sub>O<sub>5</sub> and observed a red shift of the plasmonic peak. Suspecting that a simultaneous formation of Au NPs and growth of oxide during the single annealing step during sample fabrication could have caused embedding of the Au NP in the Ta<sub>2</sub>O<sub>5</sub> oxide, we further investigated the absorbance spectra of Au NP on planar Ta<sub>2</sub>O<sub>5</sub>, on Ta<sub>2</sub>O<sub>5</sub> dimples produced by a two-step annealing procedure, and on quartz glass; these results are shared in Figures S6, S7, and Section S2 of the Supporting Information and show that a one-step annealing of a dimpled surface results in the greatest red shift of the LSPR of Au NP.

Since the plasmonic enhancement of the local electromagnetic field is inversely proportional to the LSPR peak width, broadening of the surface plasmon resonance feature is undesirable. We observed a narrowing of the dipolar surface plasmon extinction band with the LSPR full width at half-maximum (fwhm) decreasing from 0.64 eV for Au NPs on

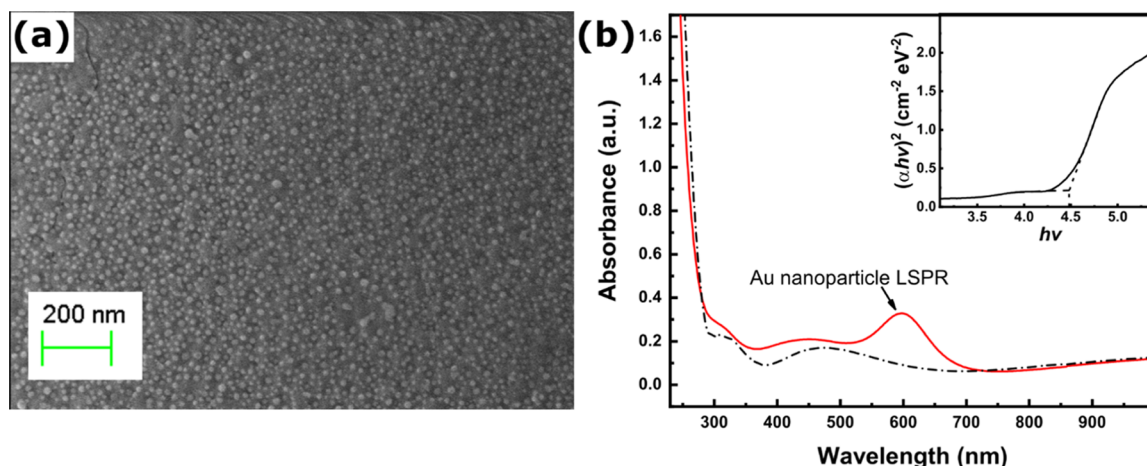


**Figure 6.** (a) HIM image of Au NPs on Ta<sub>2</sub>O<sub>5</sub> nanodimples. (b) UV–vis spectra of Ta<sub>2</sub>O<sub>5</sub> nanodimples (black dashed line) and Au NPs on Ta<sub>2</sub>O<sub>5</sub> nanodimples (red solid line). Inset shows the Tauc plot of Ta<sub>2</sub>O<sub>5</sub> nanodimples.

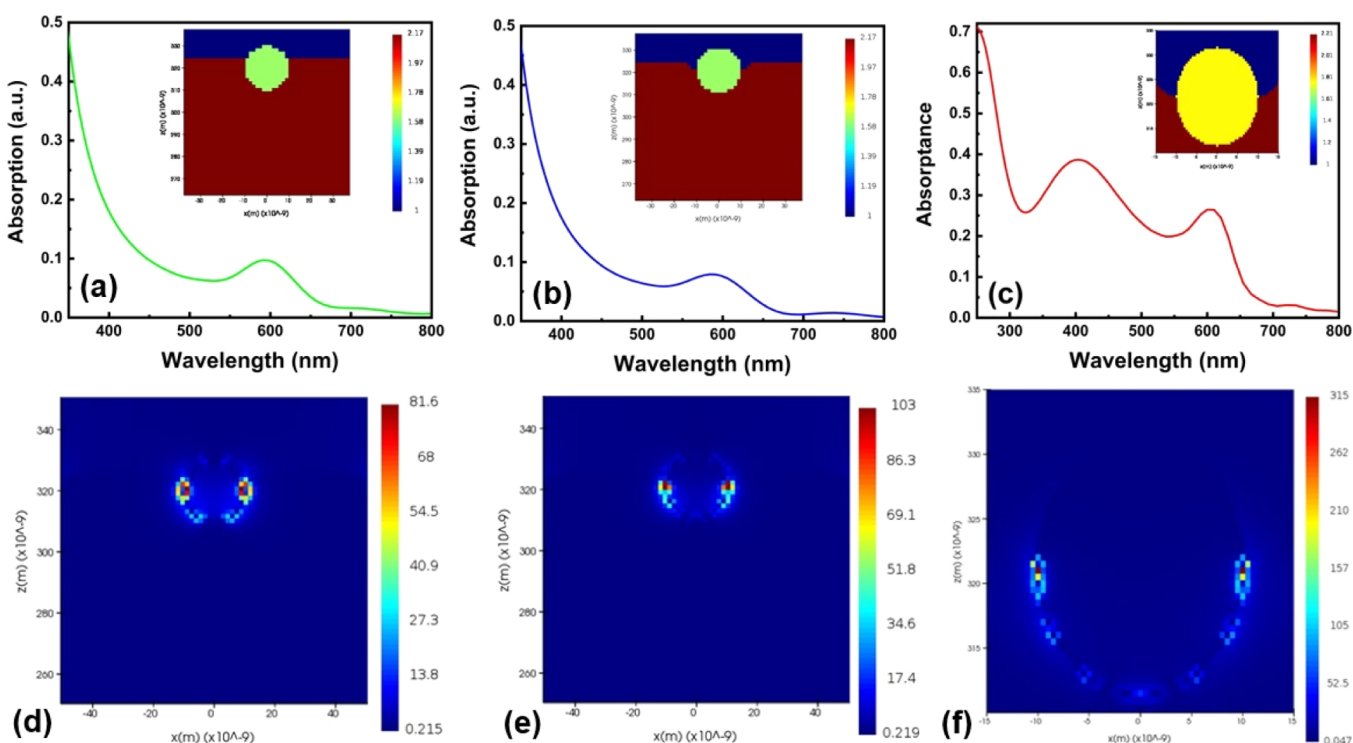


**Figure 7.** Simulated optical properties of possible Au NP/Ta<sub>2</sub>O<sub>5</sub> nanodimple configurations. (a–c) Simulated absorption spectra with the corresponding insets indicating the refractive index profile, and (d–f) Corresponding electric field intensities along the *xy* plane corresponding to the substrate surface. Light was normally incident on the *xy* plane. The figures are arranged so that each column corresponds to a different simulation, that is, (a,d) correspond to the same simulation.

glass to an fwhm value of 0.44 eV for Au NPs on Ta<sub>2</sub>O<sub>5</sub> nanodimple arrays (Figure S6 in the Supporting Information), which may be attributed to a narrower size distribution as evidenced by NP imaging, described in Section S2 and shown in Figures 6 and S7. Spontaneous solid-state dewetting of the Au film is driven by a reduction in surface energy through elimination of the Au–Ta<sub>2</sub>O<sub>5</sub> interface since Au wets metal oxides poorly (recall that a thin native oxide is expected to be present even on Ta dimples).<sup>50–52</sup> The creation of an ordered array of nanodimples produces a periodic variation in the curvature of the substrate. The process of dewetting of the vacuum-deposited Au film, which would normally commence from grain boundaries, random voids, and other such defects,

instead proceeds from areas with sharply changing curvature. Periodic variation in the structural curvature also limits diffusion paths once dewetting is underway and enables the formation of NPs with a narrower size distribution and well-defined spacing. Thus, the ordered array of nanodimples acts as a template for the controlled solid-state dewetting of the Au film. Such periodic topographic modification of the substrate has been previously shown to produce monodisperse, ordered arrays of metal NPs subsequent to controlled dewetting of vacuum-deposited metal films.<sup>53,54</sup> Consequently, the quality factor (*Q*) of the resonance given by  $\omega_p/\text{fwhm}$  for the Au NPs observed here increases by 27% from 3.7 on glass to 4.7 on Ta<sub>2</sub>O<sub>5</sub> nanodimples.

We were unable to obtain clear scanning electron microscopy (SEM) images of the cross section of the material at a magnification suitable to resolve Au NPs and prove embedding directly; thus, the optical properties of the bare and Au NP-coated Ta<sub>2</sub>O<sub>5</sub> nanodimples were investigated using FDTD electromagnetic simulations. The dimples were simulated using three different specifications of pore diameters and depths corresponding to anodization voltages of 15, 30, and 40 V, based on the pore dimensions observed in Figure 4. For anodization voltages of 15, 30, and 40 V, we used pore diameters of 25, 30, and 40 nm, respectively, and pore depths of 2, 5, and 9 nm, respectively, to construct the simulation geometry. Index monitors were utilized to provide refractive index mapping of the simulated structures, as shown in Figure S8a–c in the Supporting Information, and helped confirm that the nanodimples were appropriately configured and identified by the software throughout the course of the simulation. Figure S8d shows the simulated absorption spectra of the Ta<sub>2</sub>O<sub>5</sub> nanodimples, which reproduced the sharp band edge at ~300 nm and interferometric fringes seen in the experimental spectra (Figure 6b). The interference fringe red-shifts slightly as the size of the nanodimple decreases. This is probably caused by the changing local thickness of the film owing to the dimple size.

In the simulations, merely decorating the surface of planar Ta<sub>2</sub>O<sub>5</sub> or Ta<sub>2</sub>O<sub>5</sub> nanodimples with Au NPs could not reproduce the experimentally observed optical spectra. More specifically, the observed red shift of the LSPR peak was too small and could not account for the 600 nm LSPR peak shown in Figure 6b. Within the simulations, partially embedding isolated Au NPs inside planar Ta<sub>2</sub>O<sub>5</sub> (Figure 7a) or Ta<sub>2</sub>O<sub>5</sub> nanodimples (Figure 7b) was able to reproduce the 600 nm LSPR peak. The corresponding electric field profiles (Figure 7e,f) show the most intense field enhancement (hot spots) close to the three-component (air/gold/Ta<sub>2</sub>O<sub>5</sub>) interface. However, Figure 7a,b misses the interference fringes and sharp band edge at ~300 nm (due to the Ta<sub>2</sub>O<sub>5</sub> electronic transition), observed in Figure 6b. The LSPR maximum is much broader than what is experimentally observed, and they also indicate the 350–550 nm spectral range to be dominated by a monotonically increasing absorption due to the gold interband transition, which differs from the spectra of real samples. When an array of Au NPs was partially embedded in Ta<sub>2</sub>O<sub>5</sub> nanodimple arrays, the simulated absorption spectrum (Figure 7c) reproduced all the key features seen in the experimental optical spectrum (Figure 6b) such as the 300 nm band edge, the LSPR peak at 600 nm, the relatively narrow LSPR peak width, and the presence of interferometric maxima and minima along with their approximate spectral location. The corresponding electric field profile is shown in Figure 7f.

**3.4. Au–Ta<sub>2</sub>O<sub>5</sub> Plasmonic Photocatalysis.** The Au NP-coated Ta<sub>2</sub>O<sub>5</sub> nanodimples were examined for use in plasmonic visible light-driven photocatalysis. The conversion of PATP to DMAB is studied. The photocatalytic reaction is powered by the laser in a Raman microscope; the resulting SERS signal is measured, which allows for immediate feedback of the experimental results. The Raman spectra of reference PATP and DMAB are shown in Figure 7, with signature a<sub>1</sub> modes of PATP occurring at 1085 and 1593 cm<sup>-1</sup> and the signature a<sub>g</sub> modes of DMAB occurring at 1140 and 1438 cm<sup>-1</sup> due to the vibrations of the –N=N– azo bond in DMAB.<sup>55,56</sup> It should be noted, however, that some DMAB peaks occur close to the characteristic PATP peaks, at 1082 and 1582 cm<sup>-1</sup>.

The results of the surface reaction of PATP on bare Ta<sub>2</sub>O<sub>5</sub> nanodimples, Au NPs, and Au-NP-decorated Ta<sub>2</sub>O<sub>5</sub> nanodimples are also shown in Figure 8. Bare Ta<sub>2</sub>O<sub>5</sub> nanodimples

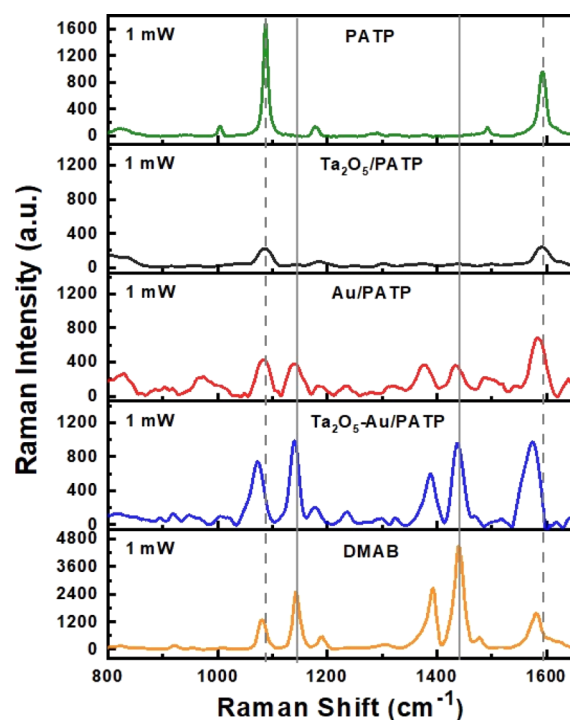


**Figure 8.** Raman spectra (top to bottom) of reference PATP (green), photo-oxidation results of PATP on bare Ta<sub>2</sub>O<sub>5</sub> nanodimples (black), Au NPs on quartz (red), Au NPs on Ta<sub>2</sub>O<sub>5</sub> nanodimples (blue), and reference DMAB (gold). Dashed lines show characteristic peaks of PATP, and solid lines show characteristic peaks of DMAB.

show almost no conversion of PATP, as would be expected, given the low light absorption of these samples; the intensity of the Raman signal at 1438 cm<sup>-1</sup> is extremely weak and does not rise above the noise in the spectrum. Au NPs show a modest conversion of PATP to DMAB, with relatively weak PATP and DMAB peaks appearing in the spectrum. When Ta<sub>2</sub>O<sub>5</sub> nanodimples are decorated with Au NPs, we observe the most efficient conversion of PATP to DATB, with strong DATB peaks similar to the reference DATB sample appearing throughout and PATP peaks either completely vanishing or weak enough to be overlapped by stronger DMAB peaks. The evolution of PATP to DATB for the latter two samples is also monitored by varying the laser power from 0.1 to 2 mW and is shown in Figure 7. As Raman laser power increases, we observe increasing amounts of conversion of PATP to DATB based on the stronger Raman signal. The ratio of the intensity of the 1140 cm<sup>-1</sup> peak (a<sub>g</sub> mode of DMAB) to the 1080 cm<sup>-1</sup> peak (a<sub>1</sub> mode of PATP) is widely used as a measure of the yield for DMAB formation.<sup>57,58</sup> For Au NPs on quartz, this ratio increases from 0.10 at a laser power of 0.1 mW to 0.73 at a laser power of 2 mW (Figure 9a). For Ta<sub>2</sub>O<sub>5</sub>–Au, this ratio increases from 0.16 at a laser power of 0.1 mW to 1.18 at a laser power of 2 mW (Figure 9b). Considering the 1 mW laser power, a 40% increase in product yield is obtained for photoconversion using the Ta<sub>2</sub>O<sub>5</sub>–Au composite compared to Au NPs on quartz; these increased product yields may be attributed to the red shift in the LSPR of Au NPs on Ta<sub>2</sub>O<sub>5</sub> which increases absorption of the 633 nm laser light and—

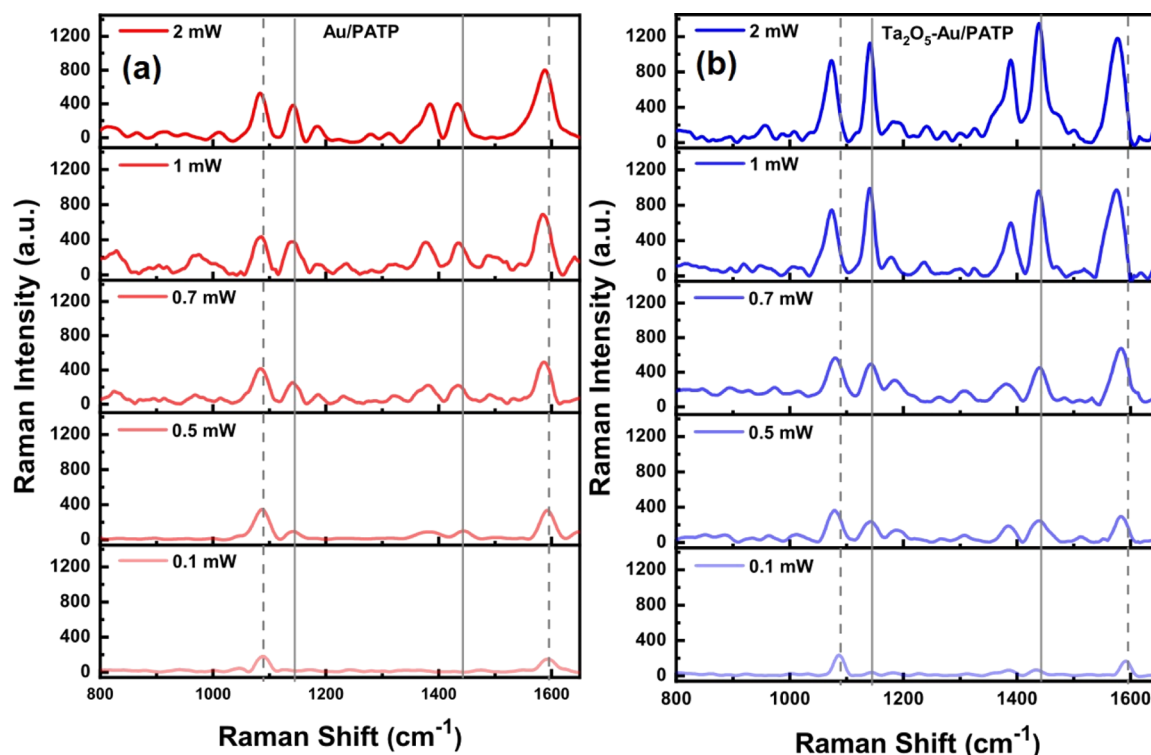


**Figure 9.** (a) Photo-oxidation results of PATP on Au NPs on quartz across differing Raman laser intensities, and (b) photo-oxidation results of PATP on Au NPs on Ta<sub>2</sub>O<sub>5</sub> nanodimple arrays across differing Raman laser intensities. Dashed lines show characteristic peaks of PATP, and solid lines show characteristic peaks of DMAB.

assuming NP embedding is indeed occurring—a large Au–Ta<sub>2</sub>O<sub>5</sub> surface contact area and thus enhanced charge separation.<sup>59</sup>

The magnitude of the local electromagnetic field enhancement ( $E_{10c}/E_0$ ) is directly proportional to  $Q$ . Thus, based on the  $Q$  reported in Section 3.2, the ratio of the ensemble-averaged field enhancement factors for Au NP-decorated Ta<sub>2</sub>O<sub>5</sub> nanodimple arrays to Au NPs on quartz is 1.27. The LSPR-mediated Raman scattering signal enhancement is roughly proportional to  $|E_{10c}/E_0|^4 \sim 2.6$ . Figure 8 shows an enhancement in the intensity of Raman modes at 1140, 1388, and 1434 cm<sup>-1</sup> corresponding to the  $a_g$  modes of DMAB for the Au NP-decorated Ta<sub>2</sub>O<sub>5</sub> nanodimple arrays (blue curve) over and above Au NPs on quartz (red curve) for a laser power of 1 mW. The Raman modes of PATP at 1090 and 1590 cm<sup>-1</sup> are also seen to be stronger in the Ta<sub>2</sub>O<sub>5</sub>–Au spectrum. This behavior suggests a strong SERS enhancement of the Raman signals for the Ta<sub>2</sub>O<sub>5</sub>–Au sample. The exact ratio(s) of the peak amplitudes of the Ta<sub>2</sub>O<sub>5</sub>–Au/PATP:Au/PATP spectra (Figure 8) for the 1140 and 1440 cm<sup>-1</sup> peaks is(are) 2.62 and 2.65, respectively, appearing to closely track the values expected from the observed field enhancement. The ratio(s) of the peak amplitudes of the Ta<sub>2</sub>O<sub>5</sub>–Au/PATP:Au/PATP spectra for the 1090, 1394, and 1590 cm<sup>-1</sup> peaks are 1.72, 1.61, and 1.42, respectively. However, it is the  $a_1$  modes (peaks at 1090 and 1590 cm<sup>-1</sup>) which are most influenced by the LSPR field enhancement and whose intensities are typically considered when quantifying this enhancement.<sup>60</sup> We note that a selective intensification of the Raman modes at 1140 and 1440 cm<sup>-1</sup> (as observed in this work) is usually attributed to a chemical enhancement.<sup>56</sup> This suggests that some chemical enhancement due to the Ta<sub>2</sub>O<sub>5</sub> surface might also be present

in addition to the plasmonic field enhancement, as has been reported by Yang et al.<sup>61</sup>

Another striking feature of the Raman spectra is the differing peak shifts observed for Au/PATP and Ta<sub>2</sub>O<sub>5</sub>–Au/PATP. For instance, the 1394 and 1440 cm<sup>-1</sup> peaks of bulk DMAB are red-shifted to 1377 and 1434 cm<sup>-1</sup>, respectively, following PATP conversion on bare Au NPs (red curve in Figure 8) but are hardly shifted in the corresponding product peaks of Ta<sub>2</sub>O<sub>5</sub>–Au/PATP (blue curve in Figure 8). Likewise, the 1087 and 1593 cm<sup>-1</sup> peaks of bulk PATP (which show up at 1082 and 1582 cm<sup>-1</sup> in bulk DMAB, respectively), are shifted to 1073 and 1575 cm<sup>-1</sup>, respectively, for Ta<sub>2</sub>O<sub>5</sub>–Au/PATP (blue curve in Figure 8). Furthermore, the magnitudes of these red shifts are negligible at small laser power and become larger with increasing laser power, as shown in Figure 9, thus ruling out the possibility of molecule chemisorption being the reason for these shifts. On the other hand, these same peaks are hardly shifted in Au/PATP even at high laser power (Figure 9a).

Studies of the mechanism of plasmon-driven photocatalysis are ongoing, and a complete understanding is still out of reach, given the intertwined complexity of the multiple processes involved. However, it has been shown that a key step is the photoactivation of reactant species by injection of plasmonic hot carriers, which are created via Landau damping of the surface plasmons.<sup>62</sup> Two mechanisms have been proposed for this reaction: the activation of triplet oxygen by generated hot electrons which oxidize the thiols or the oxidation of the thiols by hot holes.<sup>60,63</sup> Regardless of the mechanism, it is well understood that the lifetime of hot carriers is extremely short, ranging from time scales of femtoseconds to picoseconds.<sup>64</sup> This means that effective extraction of the hot carriers, before they undergo relaxation, is critical to an efficient photocatalytic reaction. Huang et al. observed a complete disappearance of

the DMAB signal in the Raman spectra of PATP-coated Au@SiO<sub>2</sub> core-shell NPs under 532 and 633 nm laser illumination due to the inability of the SiO<sub>2</sub>-coated Au NPs to activate <sup>3</sup>O<sub>2</sub> into singlet oxygen (<sup>1</sup>O<sub>2</sub>).<sup>60</sup> The SiO<sub>2</sub> shell also likely inhibits the other reaction pathway involving hot hole injection into PATP. Our simulation results indicate the Au NPs to be partially embedded in Ta<sub>2</sub>O<sub>5</sub>, decreasing the number of directly adsorbed PATP molecules on Au. In spite of this, no reduction in the PATP to DMAB conversion was observed; in fact, the DMAB signal for Ta<sub>2</sub>O<sub>5</sub>-Au/PATP was almost three times higher than that of Au/PATP, as explained earlier. Therefore, the activation of the vapor phase or adsorbed oxygen on Ta<sub>2</sub>O<sub>5</sub> by hot electrons injected from Au is highly plausible.<sup>65–67</sup> Adsorbed oxygen on Ta<sub>2</sub>O<sub>5</sub> has been previously used as a reactant in the catalytic oxidation of ethanol into acetaldehyde over Ta<sub>2</sub>O<sub>5</sub> surfaces.<sup>68</sup> Zhan et al. observed the activation of oxygen by hot electrons injected from Au into TiO<sub>2</sub> in Au/PATP/Au@TiO<sub>2</sub> NPs wherein the TiO<sub>2</sub> behaved as a charge transfer mediator.<sup>69</sup> Molecular oxygen strongly adsorbs on the surfaces of oxygen-deficient wide-band-gap transition metal oxides such as TiO<sub>2</sub>, ZnO, and Ta<sub>2</sub>O<sub>5</sub> and is responsible for persistent photoconductivity in these materials.<sup>70–73</sup>

#### 4. CONCLUSIONS

$\beta$ -Ta<sub>2</sub>O<sub>5</sub> nanodimple arrays with an electronic band gap of 4.5 eV and a bulk plasmon resonance at 21.4 eV are formed by anodizing Ta thin films on a non-native quartz substrate, delaminating the formed Ta<sub>2</sub>O<sub>5</sub> nanotubes, and then annealing. This method of self-organized synthesis produces an ordered nanodimpled surface without the use of optical or electron beam lithography. Ordered Ta nanodimples result when an anodizing range of 15–40 V is used, and 2D-FFT analysis indicated the ordering to maintain after oxidation to Ta<sub>2</sub>O<sub>5</sub>. We find that the pore diameter and depth linearly increase with anodizing voltage. At a consistent anodizing voltage, the produced film thickness is a function of anodizing time and increases predictably according to the PBR with annealing. We found an experimental ratio of 2.43, which agrees well with the theoretical value of 2.47. A double-anodizing process may be used in lieu of annealing, in cases where elevated annealing temperatures are undesirable. Coating the Ta nanodimples with a gold film and annealing the composite produce Au NP-coated Ta<sub>2</sub>O<sub>5</sub> nanodimple arrays with a relatively narrow LSPR at 600 nm, red-shifted by 75 nm from the LSPR maximum of Au NPs on SiO<sub>2</sub>. FDTD modeling of the observed optical properties suggests the Au NPs to be at least partially embedded in the Ta<sub>2</sub>O<sub>5</sub>. The resulting Au-Ta<sub>2</sub>O<sub>5</sub> nano-heterojunctions produced an elevated photocatalytic response, with a nearly 40% improvement in product yield compared to Au NPs on quartz when used for the conversion of PATP to DMAB under a 1 mW power 633 nm Raman laser.

#### ■ ASSOCIATED CONTENT

##### Supporting Information

The Supporting Information is available free of charge at <https://pubs.acs.org/doi/10.1021/acsami.0c18580>.

SEM images of delaminated Ta<sub>2</sub>O<sub>5</sub> nanotubes, anodization current density–time plots, details of the secondary anodization process to obtain Ta<sub>2</sub>O<sub>5</sub> dimples, XRD patterns of Ta dimples and Ta<sub>2</sub>O<sub>5</sub> dimples, EDX spectra

and the corresponding mapping of detected elements for Ta dimples, Ta<sub>2</sub>O<sub>5</sub> dimples, and Au NPs on Ta<sub>2</sub>O<sub>5</sub> dimples, further investigation of Au NPs formed by dewetting together with additional UV–vis spectra, He-ion microscopy images and histograms of Au NP size distribution, and simulated optical properties of various dimple sizes (PDF)

#### ■ AUTHOR INFORMATION

##### Corresponding Authors

Ryan Kisslinger – Department of Electrical and Computer Engineering, University of Alberta, Edmonton, Alberta T6G 1H9, Canada; [orcid.org/0000-0003-2456-396X](https://orcid.org/0000-0003-2456-396X); Email: [kissling@ualberta.ca](mailto:kissling@ualberta.ca)

Karthik Shankar – Department of Electrical and Computer Engineering, University of Alberta, Edmonton, Alberta T6G 1H9, Canada; [orcid.org/0000-0001-7347-3333](https://orcid.org/0000-0001-7347-3333); Email: [kshankar@ualberta.ca](mailto:kshankar@ualberta.ca)

##### Authors

Saralyn Riddell – Department of Electrical and Computer Engineering, University of Alberta, Edmonton, Alberta T6G 1H9, Canada

Ajay P. Manuel – Department of Electrical and Computer Engineering, University of Alberta, Edmonton, Alberta T6G 1H9, Canada

Kazi M. Alam – Department of Electrical and Computer Engineering, University of Alberta, Edmonton, Alberta T6G 1H9, Canada; Nanotechnology Research Centre, National Research Council of Canada, Edmonton, Alberta T6G 1H9, Canada

Aarat P. Kalra – Department of Physics, University of Alberta, Edmonton, Alberta T6G 1H9, Canada; [orcid.org/0000-0002-1877-0439](https://orcid.org/0000-0002-1877-0439)

Kai Cui – Nanotechnology Research Centre, National Research Council of Canada, Edmonton, Alberta T6G 1H9, Canada

Complete contact information is available at: <https://pubs.acs.org/10.1021/acsami.0c18580>

##### Notes

The authors declare no competing financial interest.

#### ■ ACKNOWLEDGMENTS

This work was supported by funding from the Natural Sciences and Engineering Research Council of Canada (NSERC) and Future Energy Systems Canada First Research Excellence Fund (CFREF). R.K. thanks NSERC and Alberta Innovates for scholarship support. A.P.M. thanks NSERC for scholarship support. All authors thank the National Research Council Canada and the University of Alberta nanoFAB for use of facilities and Shihong Xu for assistance with helium ion microscopy.

#### ■ REFERENCES

- (1) Md Jani, A. M.; Losic, D.; Voelcker, N. H. Nanoporous anodic aluminium oxide: Advances in surface engineering and emerging applications. *Prog. Mater. Sci.* **2013**, *58*, 636–704.
- (2) Prakasam, H. E.; Shankar, K.; Paulose, M.; Varghese, O. K.; Grimes, C. A. A New Benchmark for TiO<sub>2</sub> Nanotube Array Growth by Anodization. *J. Phys. Chem. C* **2007**, *111*, 7235–7241.
- (3) Allam, N. K.; Feng, X. J.; Grimes, C. A. Self-Assembled Fabrication of Vertically Oriented Ta<sub>2</sub>O<sub>5</sub> Nanotube Arrays, and

Membranes Thereof, by One-Step Tantalum Anodization. *Chem. Mater.* **2008**, *20*, 6477–6481.

(4) Kisslinger, R.; Riddell, S.; Savela, S.; Kar, P.; Thakur, U. K.; Zeng, S.; Shankar, K. Transparent nanoporous P-type NiO films grown directly on non-native substrates by anodization. *J. Mater. Sci.: Mater. Electron.* **2019**, *30*, 11327–11335.

(5) Xie, K.; Guo, M.; Huang, H.; Liu, Y. Fabrication of iron oxide nanotube arrays by electrochemical anodization. *Corros. Sci.* **2014**, *88*, 66–75.

(6) Sheasby, P. G.; Wernick, S.; Pinner, R. *Surface Treatment and Finishing of Aluminum and Its Alloys*; ASM International/Finishing Publications, Ltd.: Metals Park, OH: United States, 1987.

(7) Roy, P.; Kisslinger, R.; Farsinezhad, S.; Mahdi, N.; Bhatnagar, A.; Hosseini, A.; Bu, L.; Hua, W.; Wiltshire, B. D.; Eisenhawer, A.; Kar, P.; Shankar, K. All-solution processed, scalable superhydrophobic coatings on stainless steel surfaces based on functionalized discrete titania nanotubes. *Chem. Eng. J.* **2018**, *351*, 482–489.

(8) Tripp, T. B.; Foley, K. B. The Effect of Phosphorus Doping on the Direct Current Leakage of Anodic Oxide Films on Tantalum. *J. Electrochem. Soc.* **1990**, *137*, 2528–2530.

(9) O'Regan, B.; Grätzel, M. A low-cost, high-efficiency solar cell based on dye-sensitized colloidal TiO<sub>2</sub> films. *Nature* **1991**, *353*, 737–740.

(10) Barton, J. E.; Stender, C. L.; Li, P.; Odom, T. W. Structural control of anodized tantalum oxide nanotubes. *J. Mater. Chem.* **2009**, *19*, 4896–4898.

(11) El-Sayed, H.; Singh, S.; Kruse, P. Formation of Dimpled Tantalum Surfaces from Electropolishing. *J. Electrochem. Soc.* **2007**, *154*, C728.

(12) El-Sayed, H. A.; Birss, V. I. Versatile fabrication of self-assembled metallic nanoparticle arrays. *J. Mater. Chem.* **2011**, *21*, 18431–18438.

(13) El-Sayed, H. A.; Campbell, H. B.; Birss, V. I. Electrochemical applications of a Au nanoparticle array fabricated using highly ordered dimpled Ta templates. *Electrochim. Acta* **2013**, *112*, 845–852.

(14) Almeida Alves, C. F.; Calderon, V. S.; Ferreira, P. J.; Marques, L.; Carvalho, S. Passivation and dissolution mechanisms in ordered anodic tantalum oxide nanostructures. *Appl. Surf. Sci.* **2020**, *513*, 145575.

(15) Cerv, M.; Sarin, P.; Pernegger, H.; Vageeswaran, P.; Griesmayer, E. Diamond detector for beam profile monitoring in COMET experiment at J-PARC. *J. Instrum.* **2015**, *10*, C06016.

(16) Liu, W.-S.; Perng, T.-P. Ta<sub>2</sub>O<sub>5</sub> hollow fiber composed of internal interconnected mesoporous nanotubes and its enhanced photochemical H<sub>2</sub> evolution. *Int. J. Hydrogen Energy* **2019**, *44*, 17688–17696.

(17) Fu, W.; Zhuang, P.; OliverLam Chee, M.; Dong, P.; Ye, M.; Shen, J. Oxygen Vacancies in Ta<sub>2</sub>O<sub>5</sub> Nanorods for Highly Efficient Electrocatalytic N<sub>2</sub> Reduction to NH<sub>3</sub> under Ambient Conditions. *ACS Sustainable Chem. Eng.* **2019**, *7*, 9622–9628.

(18) Choi, J.; Jeong, T.-G.; Lee, D.; Oh, S. H.; Jung, Y.; Kim, Y.-T. Enhanced rate capability due to highly active Ta<sub>2</sub>O<sub>5</sub> catalysts for lithium sulfur batteries. *J. Power Sources* **2019**, *435*, 226707.

(19) Fudo, E.; Tanaka, A.; Kominami, H. Cocatalyst-free Plasmonic H<sub>2</sub> Production over Au/Ta<sub>2</sub>O<sub>5</sub> under Irradiation of Visible Light. *Chem. Lett.* **2019**, *48*, 939–942.

(20) Mengle, K. A.; Chae, S.; Kioupakis, E. Quasiparticle band structure and optical properties of rutile GeO<sub>2</sub>, an ultra-wide-band-gap semiconductor. *J. Appl. Phys.* **2019**, *126*, 085703.

(21) Snure, M.; Siegel, G.; Badescu, S. Scalable growth of atomically thin BN: an ultra-wide band gap material (Conference Presentation). *Light-Emitting Devices, Materials, and Applications XXIV*; SPIE, 2020; Vol. 11302.

(22) Chen, L.; Zhou, M.; Luo, Z.; Wakeel, M.; Asiri, A. M.; Wang, X. Template-free synthesis of carbon-doped boron nitride nanosheets for enhanced photocatalytic hydrogen evolution. *Appl. Catal., B* **2019**, *241*, 246–255.

(23) Xiu, X.; Zhang, L.; Li, Y.; Xiong, Z.; Zhang, R.; Zheng, Y. Application of halide vapor phase epitaxy for the growth of ultra-wide band gap Ga<sub>2</sub>O<sub>3</sub>. *J. Semicond.* **2019**, *40*, 011805.

(24) Ito, R.; Akatsuka, M.; Ozawa, A.; Kato, Y.; Kawaguchi, Y.; Yamamoto, M.; Tanabe, T.; Yoshida, T. Photocatalytic Activity of Ga<sub>2</sub>O<sub>3</sub> Supported on Al<sub>2</sub>O<sub>3</sub> for Water Splitting and CO<sub>2</sub> Reduction. *ACS Omega* **2019**, *4*, 5451–5458.

(25) Mendoza-Mendoza, E.; Nuñez-Briones, A. G.; Leyva-Ramos, R.; Peralta-Rodríguez, R. D.; García-Cerda, L. A.; Barriga-Castro, E. D.; Ocampo-Pérez, R.; Rodríguez-Hernández, J. A novel two-step route for synthesizing pure Ta<sub>2</sub>O<sub>5</sub> nanoparticles with enhanced photocatalytic activity. *Ceram. Int.* **2019**, *45*, 6268–6274.

(26) Liu, W.-S.; Liao, M.-W.; Huang, S.-H.; Reyes, Y. I. A.; Tiffany Chen, H.-Y.; Perng, T.-P. Formation and characterization of gray Ta<sub>2</sub>O<sub>5</sub> and its enhanced photocatalytic hydrogen generation activity. *Int. J. Hydrogen Energy* **2020**, *45*, 16560–16568.

(27) Farsinezhad, S.; Mohammadpour, A.; Dalrymple, A. N.; Geisinger, J.; Kar, P.; Brett, M. J.; Shankar, K. Transparent Anodic TiO<sub>2</sub> Nanotube Arrays on Plastic Substrates for Disposable Biosensors and Flexible Electronics. *J. Nanosci. Nanotechnol.* **2013**, *13*, 2885–2891.

(28) Horcas, I.; Fernández, R.; Gómez-Rodríguez, J. M.; Colchero, J.; Gómez-Herrero, J.; Baro, A. M. WsXM: A software for scanning probe microscopy and a tool for nanotechnology. *Rev. Sci. Instrum.* **2007**, *78*, 013705.

(29) Rodríguez-de Marcos, L. V.; Larruquert, J. I.; Méndez, J. A.; Aznárez, J. A. Self-consistent optical constants of SiO<sub>2</sub> and Ta<sub>2</sub>O<sub>5</sub> films. *Opt. Mater. Express* **2016**, *6*, 3622–3637.

(30) Singh, S.; Barden, W. R. T.; Kruse, P. Nanopatterning of Transition Metal Surfaces via Electrochemical Dimple Array Formation. *ACS Nano* **2008**, *2*, 2453–2464.

(31) Yasuda, K.; Macak, J. M.; Berger, S.; Ghicov, A.; Schmuki, P. Mechanistic Aspects of the Self-Organization Process for Oxide Nanotube Formation on Valve Metals. *J. Electrochem. Soc.* **2007**, *154*, C472.

(32) Pilling, N. B.; Bedworth, R. E. The oxidation of metals at high temperatures. *J. Inst. Met.* **1923**, *29*, 529–582.

(33) Xu, C.; Gao, W. Pilling-Bedworth ratio for oxidation of alloys. *Mater. Res. Innovations* **2000**, *3*, 231–235.

(34) Garcia-Vergara, S. J.; Skeldon, P.; Thompson, G. E.; Habazaki, H. A flow model of porous anodic film growth on aluminium. *Electrochim. Acta* **2006**, *52*, 681–687.

(35) Horwood, C. A.; El-Sayed, H. A.; Birss, V. I. Precise electrochemical prediction of short tantalum oxide nanotube length. *Electrochim. Acta* **2014**, *132*, 91–97.

(36) El-Sayed, H.; Singh, S.; Greiner, M. T.; Kruse, P. Formation of highly ordered arrays of dimples on tantalum at the nanoscale. *Nano Lett.* **2006**, *6*, 2995–2999.

(37) Farsinezhad, S.; Dalrymple, A. N.; Shankar, K. Toward single-step anodic fabrication of monodisperse TiO<sub>2</sub> nanotube arrays on non-native substrates. *Phys. Status Solidi A* **2014**, *211*, 1113–1121.

(38) Hirvonen, J.; Revesz, A. G.; Kirkendall, T. D. Rutherford backscattering investigation of thermally oxidized tantalum on silicon. *Thin Solid Films* **1976**, *33*, 315–322.

(39) Gates-Rector, S.; Blanton, T. The Powder Diffraction File: a quality materials characterization database. *Powder Diffr.* **2019**, *34*, 352–360.

(40) Shvets, V. A.; Aliev, V. S.; Gritsenko, D. V.; Shaimeev, S. S.; Fedosenko, E. V.; Rykhliitski, S. V.; Atuchin, V. V.; Gritsenko, V. A.; Tapilin, V. M.; Wong, H. Electronic structure and charge transport properties of amorphous Ta<sub>2</sub>O<sub>5</sub> films. *J. Non-Cryst. Solids* **2008**, *354*, 3025–3033.

(41) Peravalov, T. V.; Dolbak, A. E.; Shvets, V. A.; Gritsenko, V. A.; Asanova, T. I.; Erenburg, S. B. Atomic and electronic structure of gadolinium oxide. *Eur. Phys. J.: Appl. Phys.* **2014**, *65*, 10702.

(42) Lehovc, K. Lattice structure of β-Ta<sub>2</sub>O<sub>5</sub>. *J. Less-Common Met.* **1964**, *7*, 397–410.

(43) Bright, T. J.; Watjen, J. I.; Zhang, Z. M.; Muratore, C.; Voevodin, A. A.; Koukis, D. I.; Tanner, D. B.; Arenas, D. J. Infrared

optical properties of amorphous and nanocrystalline Ta<sub>2</sub>O<sub>5</sub> thin films. *J. Appl. Phys.* **2013**, *114*, 083515.

(44) Vos, M.; Grande, P. L.; Nandi, S. K.; Venkatchalam, D. K.; Elliman, R. G. A high-energy electron scattering study of the electronic structure and elemental composition of O-implanted Ta films used for the fabrication of memristor devices. *J. Appl. Phys.* **2013**, *114*, 073508.

(45) Tsai, H.-S.; Yang, T.-Y.; Chang, M.-T.; Chou, L.-J.; Chueh, Y.-L. Ta<sub>2</sub>O<sub>5</sub> Nanowires, Nanotubes, and Ta<sub>2</sub>O<sub>5</sub>/SiO<sub>2</sub> Core-Shell Structures: From Growth to Material Characterization. *J. Nanomater.* **2014**, *2014*, 914847.

(46) Palacio, C.; Martínez-Duart, J. M. EELS and low-energy electron emission of clean and oxygen-exposed tantalum. *Surf. Interface Anal.* **1990**, *15*, 675–680.

(47) Sethi, G.; Olszta, M.; Jing, L.; Sloppy, J.; Horn, M. W.; Dickey, E. C.; Lanagan, M. T. Structure and dielectric properties of amorphous tantalum pentoxide thin film capacitors. *2007 Annual Report—Conference on Electrical Insulation and Dielectric Phenomena, 14–17 Oct 2007, 2007*; pp 815–818.

(48) Jain, P. K.; Lee, K. S.; El-Sayed, I. H.; El-Sayed, M. A. Calculated Absorption and Scattering Properties of Gold Nanoparticles of Different Size, Shape, and Composition: Applications in Biological Imaging and Biomedicine. *J. Phys. Chem. B* **2006**, *110*, 7238–7248.

(49) Luo, Y.; Liu, X.; Tang, X.; Luo, Y.; Zeng, Q.; Deng, X.; Ding, S.; Sun, Y. Gold nanoparticles embedded in Ta<sub>2</sub>O<sub>5</sub>/Ta<sub>3</sub>N<sub>5</sub> as active visible-light plasmonic photocatalysts for solar hydrogen evolution. *J. Mater. Chem. A* **2014**, *2*, 14927–14939.

(50) Thompson, C. V. Solid-State Dewetting of Thin Films. *Annu. Rev. Mater. Res.* **2012**, *42*, 399–434.

(51) Lin, L.; Peng, X.; Mao, Z.; Li, W.; Yogeesh, M. N.; Rajeeva, B. B.; Perillo, E. P.; Dunn, A. K.; Akinwande, D.; Zheng, Y. Bubble-Pen Lithography. *Nano Lett.* **2016**, *16*, 701–708.

(52) Manuel, A. P.; Barya, P.; Riddell, S.; Zeng, S.; Alam, K. M.; Shankar, K. Plasmonic photocatalysis and SERS sensing using ellipsometrically modeled Ag nanoisland substrates. *Nanotechnology* **2020**, *31*, 365301.

(53) Giermann, A. L.; Thompson, C. V. Solid-state dewetting for ordered arrays of crystallographically oriented metal particles. *Appl. Phys. Lett.* **2005**, *86*, 121903.

(54) Wang, D.; Ji, R.; Schaaf, P. Formation of precise 2D Au particle arrays via thermally induced dewetting on pre-patterned substrates. *Beilstein J. Nanotechnol.* **2011**, *2*, 318–326.

(55) Canpean, V.; Iosin, M.; Astilean, S. Disentangling SERS signals from two molecular species: A new evidence for the production of p,p'-dimercaptoazobenzene by catalytic coupling reaction of p-aminothiophenol on metallic nanostructures. *Chem. Phys. Lett.* **2010**, *500*, 277–282.

(56) Fang, Y.; Li, Y.; Xu, H.; Sun, M. Ascertain p,p'-Dimercaptoazobenzene Produced from p-Aminothiophenol by Selective Catalytic Coupling Reaction on Silver Nanoparticles. *Langmuir* **2010**, *26*, 7737–7746.

(57) Zhong, H.; Chen, J.; Chen, J.; Tao, R.; Jiang, J.; Hu, Y.; Xu, J.; Zhang, T.; Liao, J. Plasmon catalytic PATP coupling reaction on Ag-NPs/graphite studied via in situ electrochemical surface-enhanced Raman spectroscopy. *Phys. Chem. Chem. Phys.* **2020**, *22*, 23482–23490.

(58) Ding, Q.; Li, R.; Chen, M.; Sun, M. Ag nanoparticles-TiO<sub>2</sub> film hybrid for plasmon-exciton co-driven surface catalytic reactions. *Appl. Mater. Today* **2017**, *9*, 251–258.

(59) Zhang, X.; Chen, Y. L.; Liu, R.-S.; Tsai, D. P. Plasmonic photocatalysis. *Rep. Prog. Phys.* **2013**, *76*, 046401.

(60) Huang, Y.-F.; Zhang, M.; Zhao, L.-B.; Feng, J.-M.; Wu, D.-Y.; Ren, B.; Tian, Z.-Q. Activation of Oxygen on Gold and Silver Nanoparticles Assisted by Surface Plasmon Resonances. *Angew. Chem., Int. Ed.* **2014**, *53*, 2353–2357.

(61) Yang, L.; Yang, Y.; Lombardi, J. R.; Peng, Y.; Huang, Z. Charge transfer enhancement in the surface-enhanced Raman scattering of Ta<sub>2</sub>O<sub>5</sub> superstructures. *Appl. Surf. Sci.* **2020**, *520*, 146325.

(62) Li, X.; Xiao, D.; Zhang, Z. Landau damping of quantum plasmons in metal nanostructures. *New J. Phys.* **2013**, *15*, 023011.

(63) Lin, W.; Cao, Y.; Wang, P.; Sun, M. Unified Treatment for Plasmon–Exciton Co-driven Reduction and Oxidation Reactions. *Langmuir* **2017**, *33*, 12102–12107.

(64) Zhang, Q.; Wang, H. Mechanistic Insights on Plasmon-Driven Photocatalytic Oxidative Coupling of Thiophenol Derivatives: Evidence for Steady-State Photoactivated Oxygen. *J. Phys. Chem. C* **2018**, *122*, 5686–5697.

(65) Brongersma, M. L.; Halas, N. J.; Nordlander, P. Plasmon-induced hot carrier science and technology. *Nat. Nanotechnol.* **2015**, *10*, 25–34.

(66) Manuel, A. P.; Kirkey, A.; Mahdi, N.; Shankar, K. Plexcitonics – fundamental principles and optoelectronic applications. *J. Mater. Chem. C* **2019**, *7*, 1821–1853.

(67) Zeng, S.; Vahidzadeh, E.; VanEssen, C. G.; Kar, P.; Kisslinger, R.; Goswami, A.; Zhang, Y.; Mahdi, N.; Riddell, S.; Kobryn, A. E.; Gusarov, S.; Kumar, P.; Shankar, K. Optical control of selectivity of high rate CO<sub>2</sub> photoreduction via interband- or hot electron Z-scheme reaction pathways in Au-TiO<sub>2</sub> plasmonic photonic crystal photocatalyst. *Appl. Catal., B* **2020**, *267*, 118644.

(68) Legendre, M.; Cornet, D. Catalytic oxidation of ethanol over tantalum oxide. *J. Catal.* **1972**, *25*, 194–203.

(69) Zhan, C.; Wang, Z.-Y.; Zhang, X.-G.; Chen, X.-J.; Huang, Y.-F.; Hu, S.; Li, J.-F.; Wu, D.-Y.; Moskovits, M.; Tian, Z.-Q. Interfacial Construction of Plasmonic Nanostructures for the Utilization of the Plasmon-Excited Electrons and Holes. *J. Am. Chem. Soc.* **2019**, *141*, 8053–8057.

(70) Zarifi, M. H.; Mohammadpour, A.; Farsinezhad, S.; Wiltshire, B. D.; Nosrati, M.; Askar, A. M.; Daneshmand, M.; Shankar, K. Time-Resolved Microwave Photoconductivity (TRMC) Using Planar Microwave Resonators: Application to the Study of Long-Lived Charge Pairs in Photoexcited Titania Nanotube Arrays. *J. Phys. Chem. C* **2015**, *119*, 14358–14365.

(71) Bao, J.; Shalish, I.; Su, Z.; Gurwitz, R.; Capasso, F.; Wang, X.; Ren, Z. Photoinduced oxygen release and persistent photoconductivity in ZnO nanowires. *Nanoscale Res. Lett.* **2011**, *6*, 404.

(72) Zhang, J.-Y.; Boyd, I. W. Thin tantalum and tantalum oxide films grown by pulsed laser deposition. *Appl. Surf. Sci.* **2000**, *168*, 234–238.

(73) Talip, M. A. A.; Khairir, N. S.; Kadir, R. A.; Mamat, M. H.; Rani, R. A.; Mahmood, M. R.; Zoolfakar, A. S. Nanotubular Ta<sub>2</sub>O<sub>5</sub> as ultraviolet (UV) photodetector. *J. Mater. Sci.: Mater. Electron.* **2019**, *30*, 4953–4966.

# SUPPORTING INFORMATION

## Non-lithographic formation of Ta<sub>2</sub>O<sub>5</sub> nanodimple arrays using electrochemical anodization, and their use in plasmonic photocatalysis for enhancement of local field and catalytic activity

Ryan Kisslinger<sup>a</sup>, Saralyn Riddell<sup>a</sup>, Ajay P. Manuel<sup>a</sup>, Kazi M. Alam<sup>a, c</sup>, Aarat P. Kalra<sup>b</sup>, Kai Cui<sup>c</sup> and Karthik Shankar<sup>a</sup>

<sup>a</sup>Department of Electrical and Computer Engineering, University of Alberta, 9211 - 116 St, Edmonton, Alberta, Canada

<sup>b</sup>Department of Physics, University of Alberta, 9211 - 116 St, Edmonton, Alberta, Canada

<sup>c</sup>Nanotechnology Research Centre, National Research Council of Canada, Edmonton, Alberta, Canada

\*Authors to whom correspondence should be addressed:

1. Karthik Shankar ([kshankar@ualberta.ca](mailto:kshankar@ualberta.ca))
2. Ryan Kisslinger ([kissling@ualberta.ca](mailto:kissling@ualberta.ca))

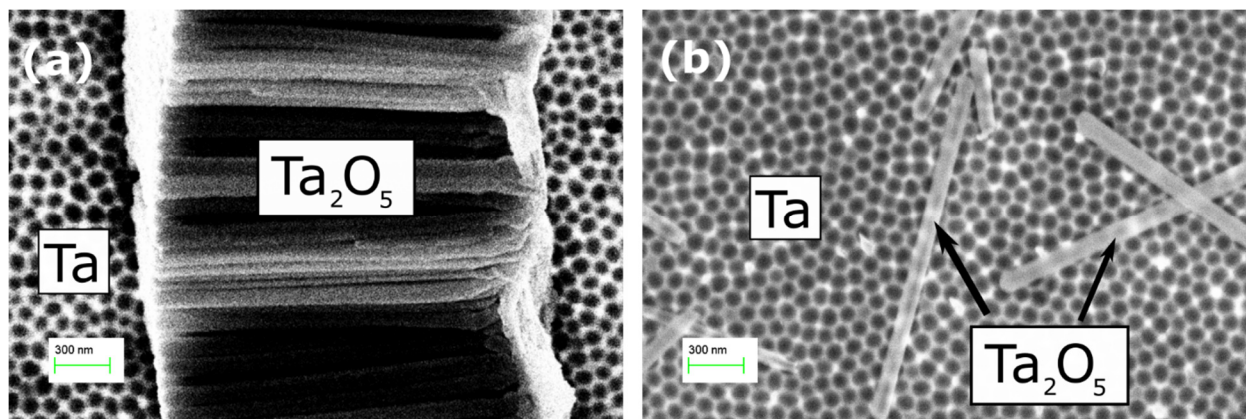


**Figure S1.** SEM Images of delaminated Ta<sub>2</sub>O<sub>5</sub> nanotubes. (a) shows an array of Ta<sub>2</sub>O<sub>5</sub> nanotubes laying on top of Ta dimples. (b) shows discrete Ta<sub>2</sub>O<sub>5</sub> nanotubes laying on top of Ta dimples, with the Ta dimples directly labelled and the drawn arrows directing to the nanotubes.

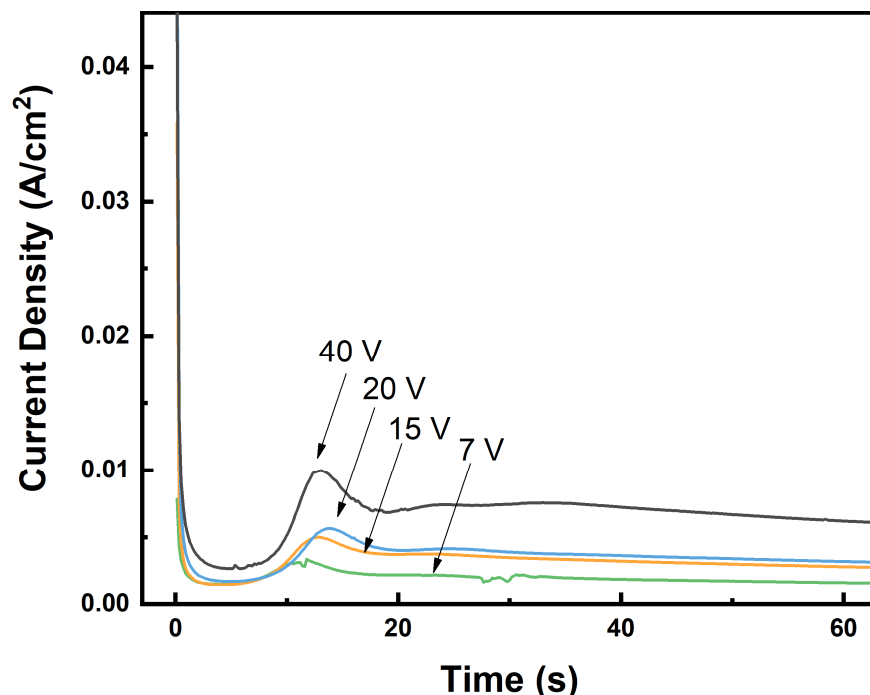


**Figure S2.** Current Density-Time plots of Ta<sub>2</sub>O<sub>5</sub> Nanotube Anodizations

### Section S1. Secondary Anodization Process to Obtain Ta<sub>2</sub>O<sub>5</sub> Dimples

It is possible to obtain Ta<sub>2</sub>O<sub>5</sub> dimples by a second anodization conducted after the first anodization, after the obtained nanotubes have been removed. This converts Ta to Ta<sub>2</sub>O<sub>5</sub> without producing pores itself and is usually referred to as a compact layer anodization.

When anodizing to obtain a compact layer, it should be recognized that there is a practical maximum thickness that can be obtained, related to the breakdown voltage of the oxide film. Oxide growth proceeds by field aided ion transport, as O<sup>2-</sup> ions react with oxidized metal ion species. As the oxide layer grows thicker and thicker, the electric field at the metal/oxide interface grows weaker and weaker, according to:

$$E = \frac{\Delta U}{t_{layer}}$$

where  $E$  is the field strength,  $\Delta U$  is the voltage drop across the oxide, and  $t_{layer}$  is the thickness of the oxide layer.<sup>1</sup> Assuming potentiostatic conditions, then this process is self-limiting and film formation will reach some maximum; under galvanostatic conditions, the voltage will increase as thickness grows until the breakdown voltage is reached. This breakdown voltage, easily

identifiable during anodization by effects such as electrical fluctuations and visible sparking, occurs when the voltage is sufficiently high enough to cause an electron avalanche, where electrons are accelerated to a sufficient energy to free other electrons by impact ionization. The resultant effect is that the oxide becomes electrically conductive.

In order to completely convert the approximately 100 nm of Ta into Ta<sub>2</sub>O<sub>5</sub>, anodic oxidation was conducted using potentiostatic conditions at 100 V in a 0.5 M aqueous H<sub>2</sub>SO<sub>4</sub> electrolyte. The cathode was a 3.05 mm diameter carbon rod submerged 2 cm into the electrolyte. The anode was spaced 1 cm below this cylindrical carbon rod, and the anodized area was 16 mm<sup>2</sup>. The dimpled Ta area was the area of anodization and was 16 mm<sup>2</sup>. The observed current-density–time plot obtained during anodization and the resultant Ta<sub>2</sub>O<sub>5</sub> dimples is shown in Figure S3a and S3b respectively. The current density decreased to a minimum value due to the formation of a highly resistive oxide layer without the formation of further pitting; this is expected in a compact layer anodization. There are several noticeable abnormalities in the spectrum with sudden spikes in current which might be related to gas bubble formation and release. Also, it was noted macroscopically that around 25% of the produced film consisted of a featureless oxide that might be indicative of local electropolishing. Nevertheless, across much of the film the nanodimpled surface was intact, with an oxide expansion similar to that observed in Figure 3 in the main text. This double-anodization process certainly stands to be optimized and further developed, but for the purposes of this work, we simply note that it is a viable method to obtain Ta<sub>2</sub>O<sub>5</sub> nanodimples.

o

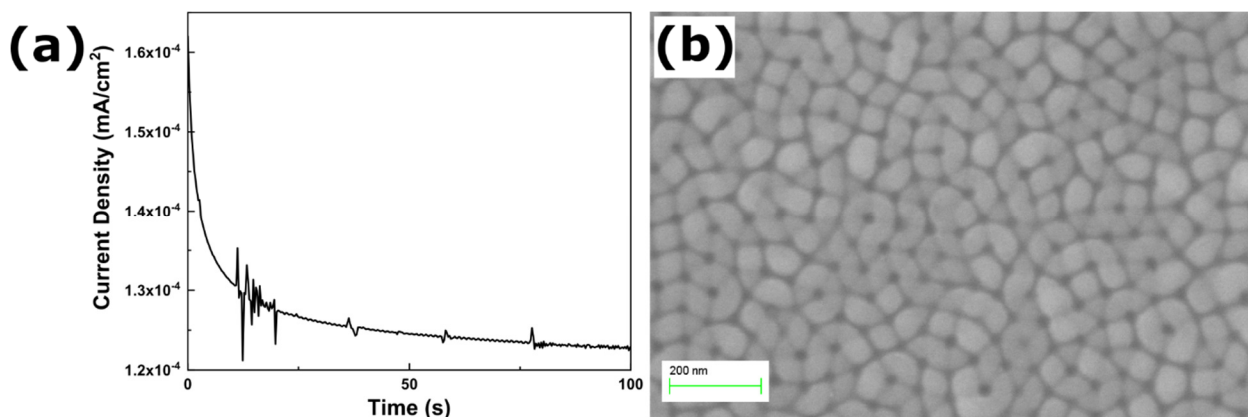


**Figure S3.** (a) Compact layer anodization to convert Ta dimples to Ta<sub>2</sub>O<sub>5</sub> (b) Ta<sub>2</sub>O<sub>5</sub> as obtained by double anodization.

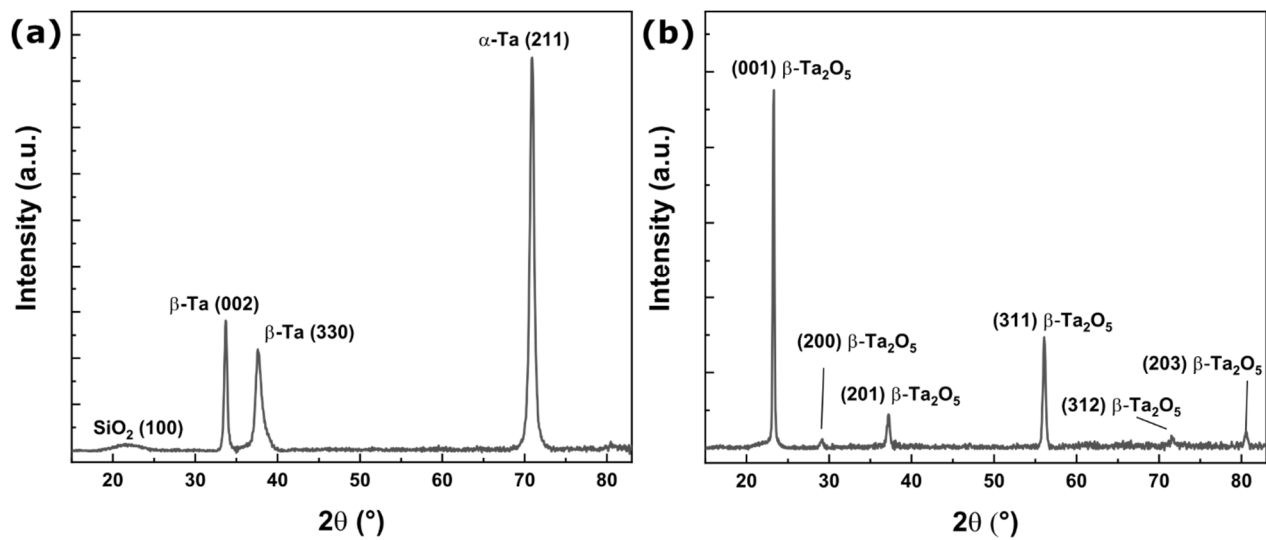


**Figure S4.** XRD patterns of (a) Ta nanodimples and (b)  $\text{Ta}_2\text{O}_5$  nanodimples. The spectrum in (a) is also representative of the sputtered Ta film before further processing.

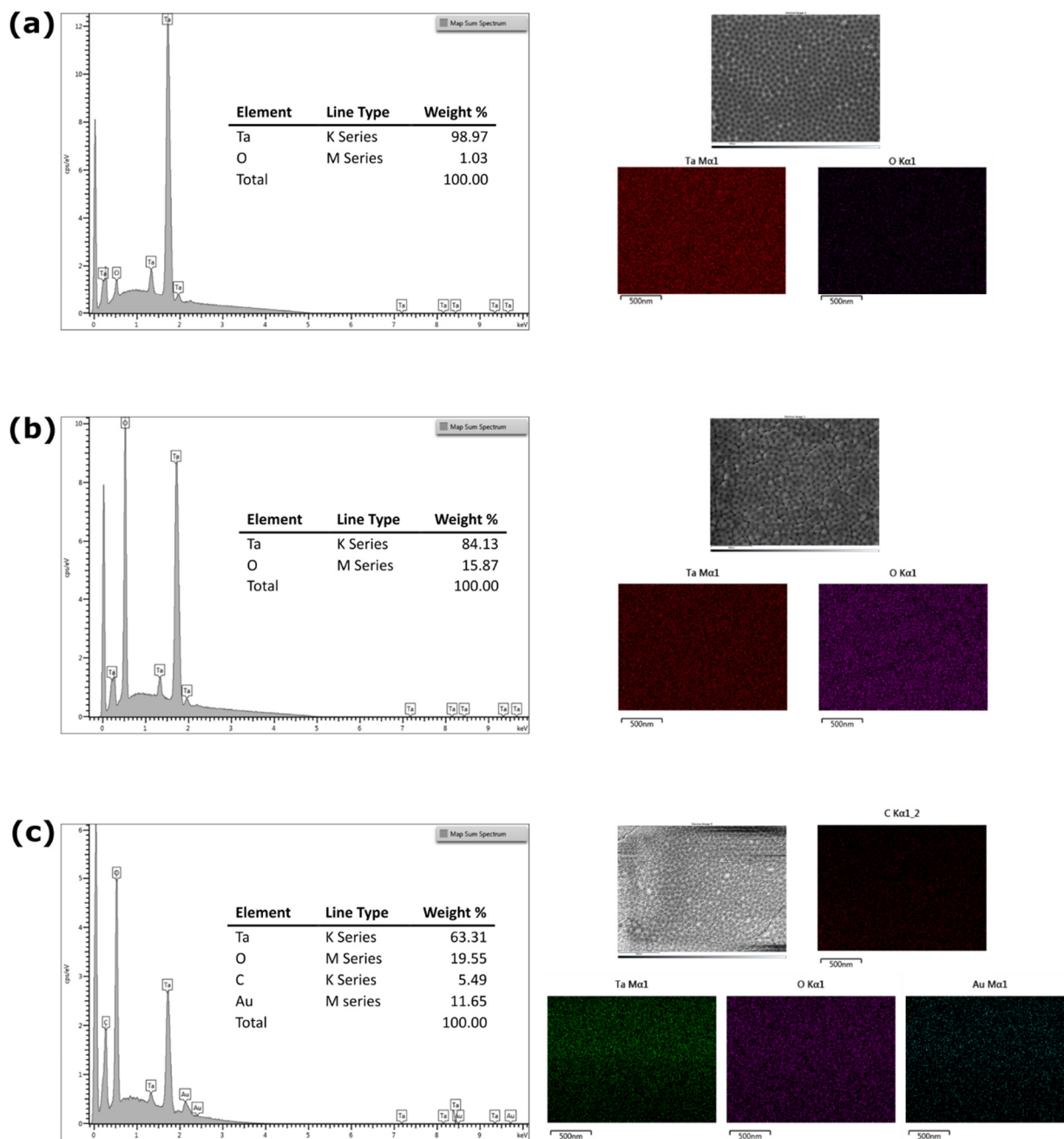


**Figure S5.** EDX Spectra and corresponding mapping of detected elements, with the inset table within the spectra showing the weight % of detected elements, for (a) Ta dimples, (b) Ta<sub>2</sub>O<sub>5</sub> dimples, and (c) Au nanoparticles on Ta<sub>2</sub>O<sub>5</sub> dimples. The low O content relative to Ta in (a) confirms that the dimples after annealing are primarily comprised of Ta, while relative O content after annealing in (b) confirms the conversion of Ta to Ta<sub>2</sub>O<sub>5</sub>, matching very closely to that expected for stoichiometric Ta<sub>2</sub>O<sub>5</sub>. For Au nanoparticles on Ta<sub>2</sub>O<sub>5</sub> dimples (c), a much higher relative O and a substantial C component is attributable to a nearby colloidal graphite conductive

paste present next to the analyzed material, used during sample preparation for FESEM imaging. The presence of Au is verified as well.

## **Section S2. Further investigation of Au nanoparticles formed by dewetting**

As mentioned in the main text of the manuscript, for the Au NP/Ta<sub>2</sub>O<sub>5</sub> composite material investigated in this study, a single annealing step is used to produce Au NPs by dewetting of a thin Au film and convert Ta dimples to Ta<sub>2</sub>O<sub>5</sub> dimples. Based on observations of red-shifting of the Au NP LSPR peak in UV-Vis spectroscopy measurements, it is suspected that a partial embedding the Au NPs in the Ta<sub>2</sub>O<sub>5</sub> NPs could be occurring. To investigate the effect of this one-step annealing process on the LSPR peak position, three types of samples were produced as a comparison. It should here be emphasized that all samples investigated in this study—with the exception of these three types of samples used for comparison in Section S2, Figure S6, and Figure S7—directly follow the Experimental section 2.4 outlined in the main text of the manuscript. The samples that directly follow Experimental section 2.4 are referred throughout Section S2, Figure S6 and Figure S7 as “One-step Annealed Au NPs on Ta<sub>2</sub>O<sub>5</sub> Dimples”.

First, Ta sputtering was conducted on quartz glass following Experimental Section 2.1. Then, an Au thin film was sputtered following Experimental section 2.4. Thermal annealing was then conducted in an identical fashion to the One-step Anneal, Ta<sub>2</sub>O<sub>5</sub> Dimples (650 °C for 30 minutes, with a 1 hour ramp up time from room temperature). These samples are hereafter referred to as “One-step Annealed Au NPs on Planar Ta<sub>2</sub>O<sub>5</sub>”.

Second, bare Ta<sub>2</sub>O<sub>5</sub> dimples were produced following Experimental Section 2.1. Then, gold sputtering was conducted following Experimental Section 2.4. Thermal annealing was then conducted in an identical fashion as the preceding paragraph. These samples are hereafter referred to as “Two-step Annealed Au NPs Ta<sub>2</sub>O<sub>5</sub> Dimples”.

Third, an Au thin film was sputtered following Experimental Section 2.4, except the substrate in this case was bare quartz glass that was cleaned following Experimental Section 2.1. Thermal annealing was then conducted in an identical fashion as the preceding paragraph. These samples are hereafter referred to as “Au NPs on Quartz Glass”.

Considering Figure S6a, the LSPR peak for Au NPs on Quartz Glass is 528 nm, which (as noted and referenced in the main text) is expected for Au NPs of this size range. In all other samples, this LSPR is relatively red-shifted owing to proximity of Ta<sub>2</sub>O<sub>5</sub> as explained in the main text. If an Au film is deposited on already-formed Ta<sub>2</sub>O<sub>5</sub> dimples and Au NPs are then formed by a second annealing step (Two-step Annealed Au NPs on Ta<sub>2</sub>O<sub>5</sub> Dimples), an LSPR peak of 576 nm is observed; in this process, embedding is unlikely as the oxide has already formed. On the other hand, if an initially planar Ta film is coated with an Au film and a one-step annealing process is used, the LSPR peak shifts to 583 nm (One-Step Annealed Au NPs on Planar Ta<sub>2</sub>O<sub>5</sub>).

Assuming the Au NP embedding theory is true, this suggests that the oxide expansion of a dimpled surface is key to the largest LSPR red-shift occurring (an LSPR peak of 600 nm is observed for One-Step Annealed Au NPs on Ta<sub>2</sub>O<sub>5</sub> dimples). A precise explanation for why a dimpled surface leads to the largest LSPR red-shift is not available at this time, but could be related to the alterations to the dewetting process that occur with a dimpled substrate morphology as detailed in the Section 3.3 of the main text. We also note that the use of a dimpled morphology appears to affect Au NP size and result in a narrower size distribution. As noted in the main text, One-step Annealed Au NPs on Ta<sub>2</sub>O<sub>5</sub> Dimples have a diameter of  $14.6 \pm 2.8$  nm based on Figure 6. Meanwhile, from Figure S7, the diameter of One-step Annealed Au NPs on Planar Ta<sub>2</sub>O<sub>5</sub> is  $20.4 \pm 2.8$  nm, the diameter of Two-step Annealed Au NPs Ta<sub>2</sub>O<sub>5</sub> Dimples is  $14.1 \pm 2.3$  nm, and the diameter of Au NPs on Quartz Glass is  $19.8 \pm 3.7$  nm. Together, these observations support the notion that a dimpled surface results in smaller Au NP sizes and a narrower size distribution. Furthermore, it is possible that embedding is more effective for the smaller Au NPs as caused by the dimpled surface, as the same relative degree of oxide expansion would envelop a greater portion of a small nanoparticle compared to a larger one.

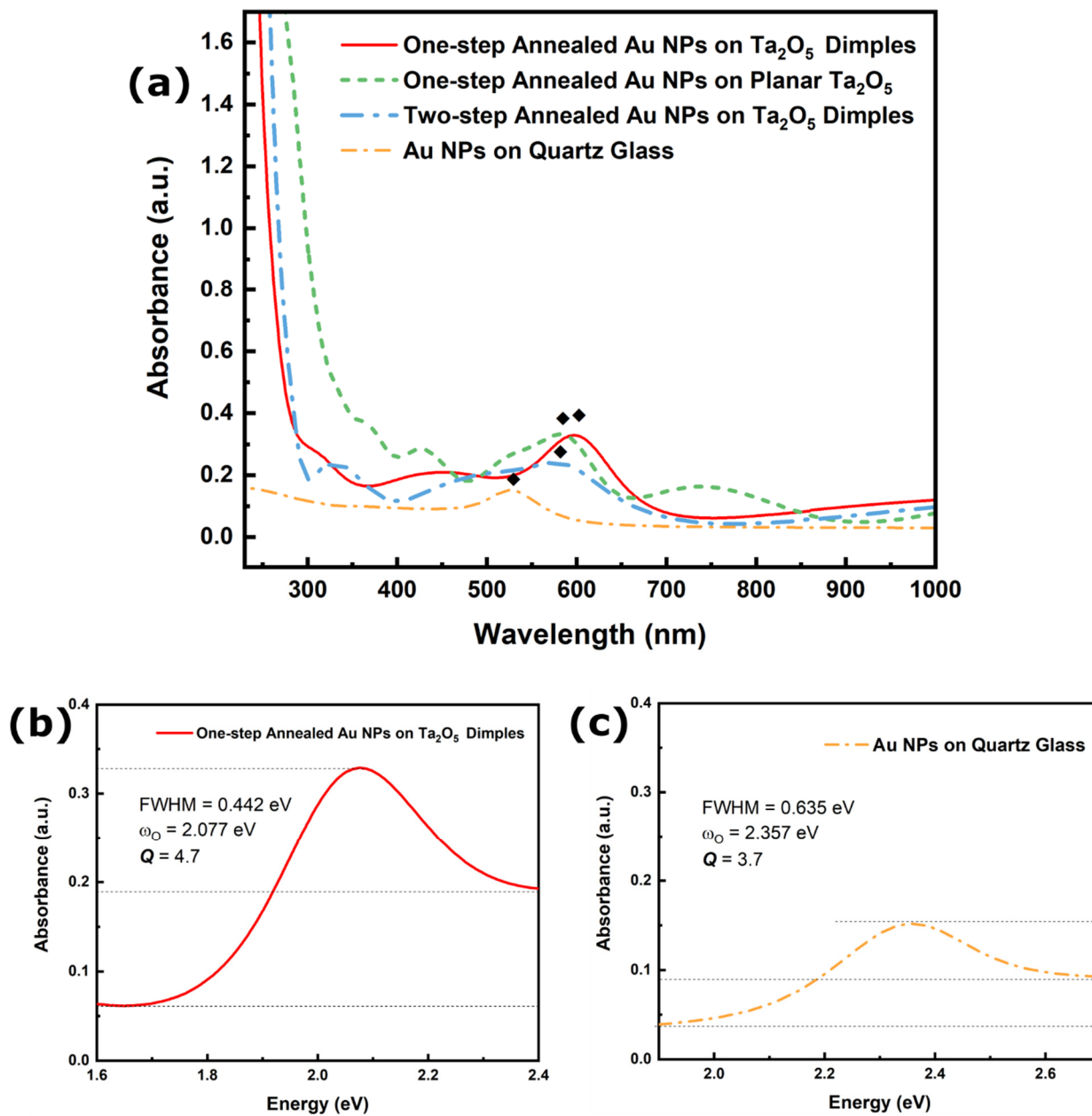


**Figure S6.** (a) UV-Vis absorption spectra of Au-nanoparticle-coated samples. The ◆ symbol indicates the LSPR peak of Au NPs for each spectrum. Note that the One-step Annealed Au NPs on Ta<sub>2</sub>O<sub>5</sub> Dimples spectrum is the same as the red curve presented in Figure 6. (b, c) Extraction of peak-width and quality factors for (b) One-step Annealed Au NPs on Ta<sub>2</sub>O<sub>5</sub> Dimples, and (c) Au NPs on Quartz Glass. Note that peak-width and quality factor were not extracted from One-Step Annealed Au NPs on Planar Ta<sub>2</sub>O<sub>5</sub> or Two-Step Annealed Au NPs on Ta<sub>2</sub>O<sub>5</sub> Dimples owing to the overlap of interference peaks.

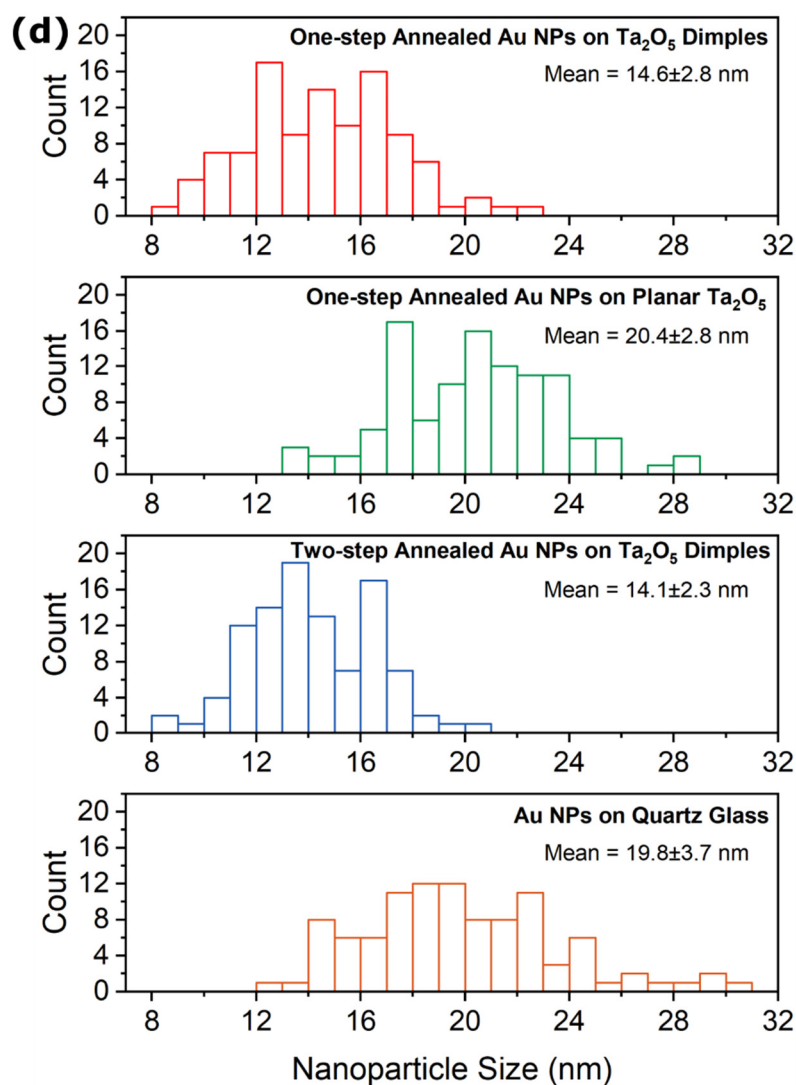
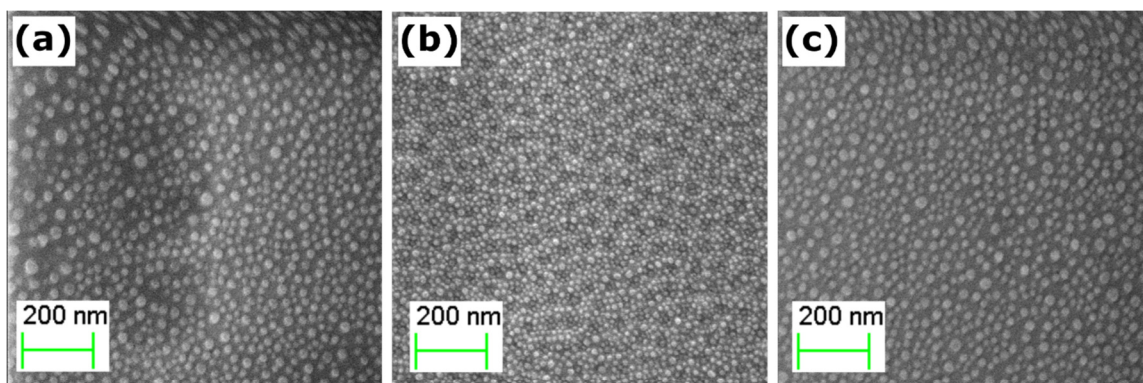


**Figure S7.** Helium Ion Microscope (HIM) images of (a) One-step Annealed Au NPs on Planar Ta<sub>2</sub>O<sub>5</sub> (b) Two-step Annealed Au NPs Ta<sub>2</sub>O<sub>5</sub> Dimples (c) Au NPs on Quartz Glass. Note that the distortion at the top of some of the images is due to sample charging. (d) shows histograms of Au NP sizes based on HIM images in Figure 6 and Figure S7a-c.

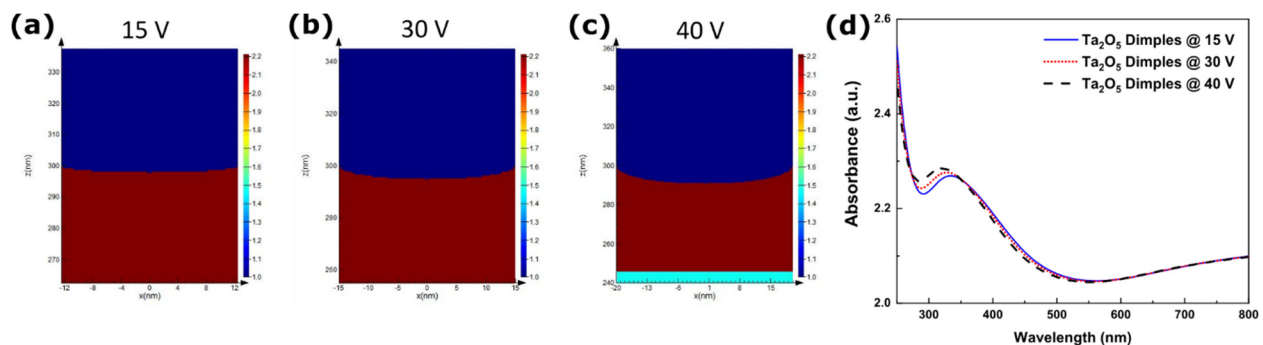


**Figure S8.** Simulated optical properties of various dimple sizes. (a)-(c) shows a schematic of the simulated dimples, while (d) is the refractive index of mapping and shows the simulated absorption spectra.

## SUPPORTING INFORMATION REFERENCES

(1) Lohregel, M. M. Thin anodic oxide layers on aluminium and other valve metals: high field regime. *Materials Science and Engineering: R: Reports* **1993**, *11* (6), 243-294, DOI: [https://doi.org/10.1016/0927-796X\(93\)90005-N](https://doi.org/10.1016/0927-796X(93)90005-N).